Measuring $\delta^{18}O$ of atmospheric oxygen for synchronizing ice core records

Master's Thesis

Written by *Rebekka Frøystad*

16. June 2016

Supervised by
Thomas Blunier

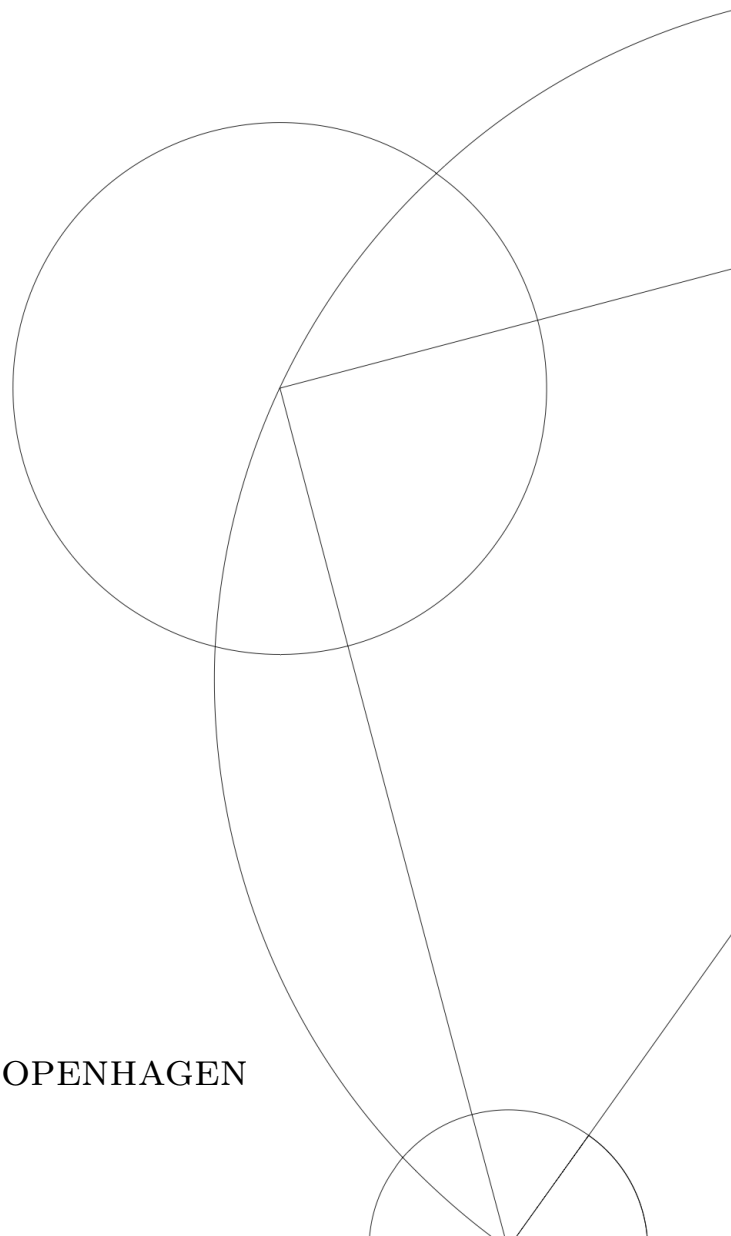

University of Copenhagen

UNIVERSITY OF COPENHAGEN

Faculty:	Faculty of Science
Institute:	The Niels Bohr Institute
Author(s):	Rebekka Frøystad
Email:	jhv901@alumni.ku.dk
Title and subtitle:	Measuring $\delta^{18}O$ of atmospheric oxygen for synchronizing ice core records -
Supervisor(s):	Thomas Blunier
Handed in:	16.06.2021
Defended:	25.06.2021

Name _____

Signature _____

Date _____

Abstract

An accurate understanding of the succession of climate events is important in the interpretation of high resolution climate records. Atmospheric oxygen (O_2) is a global tracer of biosphere productivity and can further be used to synchronize ice core records across hemispheres.

This thesis work is focused on instrumental design and optimization of an experimental setup for extracting and measuring $\delta^{18}O$ of atmospheric O_2 in ice cores.

Results from a measurement campaign of samples from the RECAP ice core are presented to verify an increase in $\delta^{18}O$ seen around 100-120 kyr BP. These data are used to further constrain the time scale for gases in the RECAP ice core by comparing them to the already established time scale for the Antarctic EDML ice core.

Contents

1 Introduction **1**

2 Background **3**

2.1 Stable isotope studies 3

2.2 Firn processes 4

2.3 The oxygen cycle 5

2.3.1 δ^{18}O and dating of ice cores 6

2.3.2 The triple oxygen isotope composition 8

2.4 Background on ice core samples 9

3 Mass spectrometry **11**

3.1 Concepts of mass spectrometry 11

3.2 Dual inlet mass spectrometry 14

3.3 Resolution 15

4 Experimental setup **16**

4.1 Requirements of setup 16

4.2 General layout for δ^{18}O measurements 17

4.3 Vacuum system 18

4.4 Sample preparation 19

4.5 Extraction system 20

4.6 Water removal 21

4.7 CO_2 removal 23

4.8 Collection unit 23

4.8.1 Cryocooler and vacuum casing 24

4.8.2 Conditioning of dip tubes 24

4.8.3 Passivation of dip tubes 24
4.9 General layout for $\delta^{17}O$ and $\delta^{18}O$ measurements 26
4.10 N_2 removal 26
4.10.1 Focusing traps 27
4.10.2 GC column 27
4.10.3 Original temperature system 28
4.10.4 A new temperature stabilization system 29
4.11 Chemical CO_2 trap 30
4.12 Automation of setup 31

5 The Delta V Plus MS **33**
5.1 Isodat NT 33
5.1.1 Measurement cycle in MS for $\delta^{18}O$ 34
5.2 Capillaries 34
5.2.1 Crimping of capillaries 34
5.2.2 Heating out capillaries 35
5.3 The ion source and focus settings 36
5.3.1 Repairing and replacing filaments 36
5.3.2 Focus settings 36
5.4 Shims and peak shapes 37
5.4.1 Peak shape dependence on extraction parameter 38

6 Corrections and instrument tests **40**
6.1 Zero-enrichment test 40
6.2 Pressure imbalance correction 42
6.3 Chemical slope measurement 44
6.4 Chemical slope for $\delta^{15}N$ 46
6.5 Mass dependent fractionation 47
6.6 Effect of CO_2 on $\delta^{18}O$ measurements 48

7 Test ice measurements and external precision **49**
7.1 Dry air measurements 49
7.2 Bubble free ice 51
7.3 NEEM and external precision 52

7.4 Uncertainty attribution 53

8 RECAP measurements **55**

8.1 Results 55

8.2 Determination of gas age 58

8.3 Discussion 61

9 Conclusion and outlook **64**

A Appendix **71**

A.1 Peak shapes 72

A.2 NEEM measurements 73

List of Figures

2.1 Illustration of the firn column and its effect on δ^{15}N. Figure is taken from [Blunier and Schwander, 2000]. 4

2.2 Main components of the oxygen cycle where F denotes the fluxes of oxygen and α is the fractionation factor for the respective process. Figure from T. Blunier. 7

2.3 Map of Greenland where drilling sites are marked with red. The shading from gray to white indicates elevation. Figure taken from [Masson-Delmotte et al., 2015]. 10

3.1 Schematic of processes in a dual inlet mass spectrometer. Figure taken from [Guillevic, 2013]. 12

3.2 Schematic of Faraday cups in the Delta V MS and the configurations used in this work. For each configuration, the m/z measured by each cup is shown. 14

4.1 Schematic of the experimental setup for δ^{18}O measurements where the N_2 separation part is excluded. Valves P0-P3 lead to the vacuum system described in figure 4.2. 18

4.2 Detailed schematic of pump system where P0 and P1 are manual valves and P2, P3 and P4 are pneumatic valves. 19

4.3 Picture of a RECAP sample that was cut at the illustrated red line to avoid contamination stemming from the visible crack in the ice. . . . 20

4.4 Photograph of glass extraction vessels along with their O-rings and connectors. Figure from Grzymala-Lubanski [2015]. 20

4.5 Detailed schematic of the two water traps. Arrows indicate the direction of gas flow and the glass beads are shown by purple circles. . . . 22

4.6 Inside of water trap, T1, after two samples have been melted and extracted. Water vapour freezes the glass beads along the walls. . . . 23

4.7 Picture from the baking of the dip tubes. Heat tape is shown to be wrapped around the aluminum cylinder. 25

4.8 Picture of complete setup for baking the dip tubes. 25

4.9 Schematic of the analytical system for triple oxygen collection. The setup consists of an extraction, purification separation and collection part. 26

4.10 Figure 2 from Barkan and Luz [2003], original caption: Chromatogram showing separation of N_2 from O_2-Ar mixture. He flow rate is $\simeq$ 25 mL·min^{-1}. 28

4.11 Picture of isolated GC column inside the freezer. The connection to the power supply for the heat tape is achieved by fitting the wires through holes drilled through the ceiling of the freezer. 29

4.12 Schematic of the chemical CO_2 trap with the direction of NEEM reference gas flow denoted by an arrow. 30

4.13 Example of visual code in LabView for timing the opening time of a control. 32

5.1 Intensity vs magnetic field. N_2/O_2/Ar configuration slow magnet scan in 2020. 37

5.2 Intensity vs magnetic field. N_2/O_2/Ar configuration slow magnet scan in 2007. 37

5.3 One of two shims placed between the magnet and the analyzer in the flight tube. 38

5.4 Vertical axes are signal intensities in mV, while the horizontal axes are the high voltage in kV. Red line is m/z 28 (cup 3), green line is m/z 29 (cup 4) and blue line is m/z 30 (cup 5). 39

6.1 Average of δ^{18}O from the zero-enrichment tests made for different measurement days. Error bars indicate the standard deviation of the mean for a certain day. 41

6.2 Average of δ^{15}N from the zero-enrichment tests made for different measurement days. Error bars indicate the standard deviation of the mean for a certain day. 41

6.3 Pressure imbalance data with a linear regression fitted to it from 01.06.2021. 43

6.4 Combined chemical slope test for 16.03.21 and 21.03.21. The data is not corrected for pressure imbalance, and the plot is merely included for illustrating the effect of kinetic fractionation in the bellows when compressed. 45

6.5 Chemical slope test from 23.03.21 where the data has been corrected for pressure imbalance effects. The errorbars indicate the standard deviation on the δ^{18}O measurement. 46

6.6 δ^{15}N is plotted as a fuction of $\delta O_2/N_2$. 47

6.7 δ^{18}O is plotted as a fuction of δCO_2. A linear fit to the data is also shown. 48

7.1 δ^{18}O for the ten rods measured at different times throughout the project. 50

7.2 δ^{18}O for rods 6,8 and 9 measured at different times throughout the project. 51

8.1 Atmospheric δ^{18}O plotted against depth for the RECAP ice core. Measurements by PSU. 55

8.2 Atmospheric δ^{18}O plotted against depth for the RECAP core. Measurements from this thesis work (NBI-PICE) are black, while from PSU are purple. 56

8.3 δ^{15}N is plotted against depth for the RECAP core. Measurements from this thesis work (NBI-PICE) are black, while from PSU are purple. . 57

8.4 The measured δ^{18}O and its corrections plotted against depth for the RECAP core. 57

8.5 In blue is the mean of 10,000 synthetic generated records where the standard deviation is shaded. The red markers indicate the measured EDML δ^{18}O against gas age. 58

8.6 Histograms generated following $P(t)$. 60

8.7 δ^{18}O of the NBI-PICE and PSU with estimated gas ages plotted alongside the synthetic record based on the EDML ice core. 61

8.8 Gas age estimates for the RECAP ice core measurements from PSU and NBI-PICE are plotted against depth. Tie markers from the GICC05 time scale are plotted for comparison. 62

A.1 Peak shapes of the N_2/O_2/Ar configuration for different values of extraction. Vertical axes are signal intensities in mV, while the horizontal axes are the high voltage in kV. 72

List of Tables

2.1 Major constituents of dry air by volume. 6

2.2 Stable isotopes of oxygen. 6

2.3 Name, drilling period and coordinates for the ice cores whose samples have been measured in the course of this project. 10

3.1 Molecules and atoms that are measured and mentioned in this work alongside their mass-to-charge ratio for $z = 1$. 13

5.1 Results of zero-enrichment measurements for different extraction values. 39

6.1 Results from PI tests over the month where the system was used for measurement of RECAP samples. The PI slope is decided by a least-square fit. 44

7.1 Standard deviations for each rod resulting from the measurements made throughout the project. 50

7.2 Measurements of δ^{18}O and δ^{15}N from reference over BFI experiments. 52

7.3 Measurements of δ^{18}O from recent Holocene NEEM ice. The gravitational corrected data is also Z.E. corrected. 53

7.4 Overview of the estimated uncertainties due to the different components of the setup. 53

8.1 Measurements obtained from the RECAP samples. 56

8.2 Gas ages for the samples are shown alongside their 95% confidence intervals. 61

A.1 Measurements of δ^{18}O and δ^{15}N from recent Holocene NEEM ice. . . 73

1 | Introduction

As snow falls in cold regions, it slowly transforms into firn and subsequently ice due to gravity and the weight of accumulating precipiation. The interior regions of large ice sheets such as those found in Greenland and Antarctica are less affected by melt, and thus preserve layers of old ice. These layers can be investigated to infer information on how environmental conditions have changed in the past. Ice cores of a few kilometers length are retrieved from the ice sheets and these deep ice cores serve as important archives of paleoenvironmental information. For example, the current oldest ice core retrieved from East Antarctica captures a detailed picture of the Earth's paleoclimate extending back around 800 000 years, that is to the Pleistoscene period [Augustin et al., 2004]. Among the climate information in ice cores, ancient air trapped in the bubbles is arguably one of the most unique paleoenvironmental archive available - as it represents actual samples of Earth's past atmosphere [Brook and Buizert, 2018].

Oxygen is the second most abundant gas in the atmosphere and plays a role in many key parts of Earth's climate system. The isotopic composition of atmospheric oxygen can be used as a proxy to infer complex biological processes. As oxygen resides in the atmosphere over a long time and mixes globally, it can also be used for relative dating of gas age in ice cores.

Overview of this thesis

The work presented in this thesis is mainly experimental with emphasis on instrumental design and optimization. The goal of the project was initially to develop a $\delta^{17}O$ measurement system for gases in ice core samples based on the method that has been successfully implemented for measuring modern air samples [Barkan and Luz, 2003].

Unfortunately, due to several unexpected technical challenges, discussed in detail in chapters 4 and 5, the complete implementation of $\delta^{17}O$ measurement system has to be delayed. Instead of fully focusing on $\delta^{17}O$, this thesis will therefore also cover the development of $\delta^{18}O$ measurement system at the Niels Bohr Institute Physics of Ice Earth and Climate's (NBI-PICE) new laboratory at Tagensvej 16 and $\delta^{18}O$ data analysis from a successful measurement campaign of the RECAP ice core [Simonsen et al., 2019].

At first, in chapter 2, background on how isotopic measurements of atmospheric oxygen in ice cores, both $\delta^{17}O$ and $\delta^{18}O$, are used to infer past biological processes is presented. Chapter 3 goes into more detail on the theory behind mass spectrometry, the method used in this project for measuring isotopic compositions.

In chapters 4 and 5, the more technical aspects of the project are discussed. Chapter 4 describes the ice extraction setup for both $\delta^{17}O$ and $\delta^{18}O$. Chapter 5 discusses the application of the mass spectrometer for $\delta^{18}O$ measurement and the challenges encountered. In these chapters, the precision, accuracy and continuity of the experimental setup are analyzed.

Chapter 6 discusses the necessary instrument corrections required to reconstruct paleoatmospheric $\delta^{18}O$.

In chapter 7, measurements of test ice are presented along with a discussion on the external precision of the setup. At the very end of the thesis, in chapter 8, new measurements of the RECAP ice core are presented alongside a discussion on how these contribute to other records and can be used for establishing a timescale for the core.

2 | Background

2.1 Stable isotope studies

Isotopes are atoms whose nuclei have the same number of protons, Z, but vary in the number of neutrons, N. Isotopes of an element, X, are therefore distinguished by being denoted as ${}^{Z+N}\mathrm{X} = {}^{M}\mathrm{X}$, making M the atom's number of nuclei. A multitude of processes in nature have been found to change the isotopic compositions of elements. Processes that alter the isotopic composition of a compound are called fractionation processes. Stable isotopes are non-radioactive atoms preserving information on these mechanisms which often represent important physical, chemical, or biological processes in nature. Therefore, stable isotope studies have been widely used to investigate and reconstruct paleoclimatic conditions.

A common and practical nomenclature is needed to be able to compare isotopic abundances by researchers across the globe. For major components of air such as N_2, O_2, and Ar, samples are therefore compared to a reference atmospheric measurement which is a sample from today's clean air. These air standards are taken from regions with negligible pollution and contamination, e.g. at polar ice caps. Typically, the compositional changes tend to be small. Therefore, to express the relative difference of the ratio compared to that of the chosen reference concentration, the "delta nomenclature", δ, is commonly used in stable isotope studies. The δ of a measured isotopic ratio in a sample, R, to its reference, R_s is defined as

$$\delta = \left[\frac{R}{R_s} - 1\right]. \tag{2.1}$$

The delta notation makes it convenient to gauge small variations of the ratios; in this work the δ values typically range between 10^{-3} and 10^{-6}. The isotopic ratios will be given as the concentrations of the heavier (minor) to the lighter (major) isotopes. As explicit examples, the ratios of ${}^{18}\mathrm{O}$ to ${}^{16}\mathrm{O}$, $\delta^{18}\mathrm{O}$, and ${}^{17}\mathrm{O}$ to ${}^{16}\mathrm{O}$, $\delta^{17}\mathrm{O}$, are given by

$$\delta^{18}\mathrm{O} = \left[\frac{({}^{18}\mathrm{O}/{}^{16}\mathrm{O})_{\mathrm{sample}}}{({}^{18}\mathrm{O}/{}^{16}\mathrm{O})_{\mathrm{reference}}} - 1\right], \quad \delta^{17}\mathrm{O} = \left[\frac{({}^{17}\mathrm{O}/{}^{16}\mathrm{O})_{\mathrm{sample}}}{({}^{17}\mathrm{O}/{}^{16}\mathrm{O})_{\mathrm{reference}}} - 1\right]. \tag{2.2}$$

The δ nomenclature is also used to express elemental ratios. For the ratio of oxygen to nitrogen in the atmosphere, their $\delta O_2/N_2$ value becomes

$$\delta O_2/N_2 = \left[\frac{(O_2/N_2)_{\text{sample}}}{(O_2/N_2)_{\text{reference}}} - 1 \right]. \tag{2.3}$$

When the isotopic ratio is changed through some chemical or physical reaction, a fractionation factor, α, for that specific reaction can be defined as

$$R_B = \alpha R_A, \tag{2.4}$$

where R_A and R_B are the isotopic ratios in the reactant and product associated with the reaction. This notation can further be used to describe the overall fractionation of several isotope exchange reactions. The fractionation effect, ϵ from a reaction can thus be defined as

$$\epsilon = \alpha - 1. \tag{2.5}$$

2.2 Firn processes

The upper 50-100 m of an ice sheet is called the firn layer. Here the transformation from snow to ice occurs by densification [Herron and Langway, 1980]. This transformation is illustrated in figure 2.1, where typical depths of the stages between snow and ice are shown.

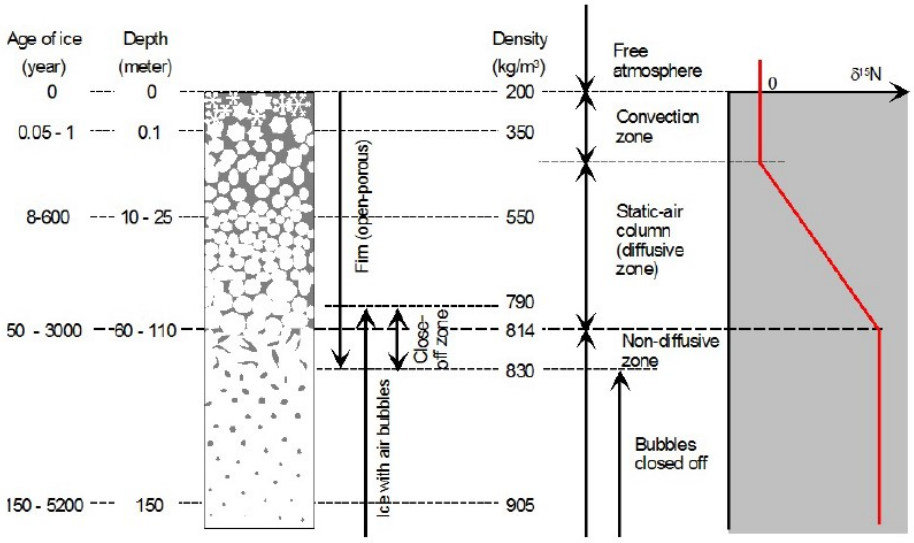

Figure 2.1: Illustration of the firn column and its effect on $\delta^{15}N$. Figure is taken from [Blunier and Schwander, 2000].

Atmospheric air diffuses freely through the pores of the firn, however, with increasing depth the gas is gradually enclosed in bubbles. A study on the Siple station drilling

site found that 80% of the bubble volume is already occluded as the firn densitiy is $795 < \rho < 830$ kg m^{-3} [Schwander and Stauffer, 1984]. In this interval, called the close-off zone, the mean close-off density, $\rho_{\overline{\text{co}}}$, is typically found, independent of accumulation rate but slightly dependent on the drilling site temperature [Martinerie et al., 1992, 1994].

Since air can diffuse down through the firn, the trapped atmospheric age is younger than that of the surrounding ice lattice at bubble close-off. The full close-off depth, z_{cod} where all bubbles are closed is typically found between 60-100 m below the surface.

Prior to bubble closure, the firn layer is the origin of processes altering the isotopic and elemental compositions of the gases trapped in ice cores. It is therefore vital to understand and account for these processes to correctly interpret measurements.

Figure 2.1 shows how δ^{15}N changes with depth in the firn column. In the uppermost part, the convection zone, the air is well mixed with the atmosphere and the isotopic ratios equal those of today's troposphere. However, in the diffusive zone, where gas transport in the smaller channels is due to molecular diffusion, the heavier elements and isotopes tend to move downward resulting in an increasing enrichment of δ^{15}N in the gas. This is due to gravity, and the isotopic change is termed gravitational fractionation. Today, the effect results in a δ^{15}N below close-off depth of $\simeq$0.27 permille for the NEEM ice core. A shorter firn column results in a smaller enrichment in δ^{15}N. Close-off depth is controlled by the firn temperature and snow accumulation [Schwander et al., 1997, Goujon et al., 2003].

Following other studies [Bender et al., 1994b, Sowers and Bender, 1995, Severinghaus et al., 2009], δ^{18}O and $\delta O_2/N_2$ can be corrected for this gravitational fractionation by

$$\delta_{\text{gravcorr}} = \delta - \Delta m \cdot \delta^{15}\text{N}, \tag{2.6}$$

where the mass difference Δm is 2 for δ^{18}O and 4 for δ^{18}O and $\delta O_2/N_2$ when using δ^{15}N for the correction. Eq. 2.6 accounts for all mass dependent fractionation processes, and so also corrects δ^{18}O for any such artifacts of the instrumental setup.

Fractionation during bubble close-off, clathrate formation and gas loss during ice core drilling and storage may still change the isotopic compositions. These are smaller corrections than those imposed by instrument effects and gravitational fractionation, but may be necessary to obtain higher accuracy on the measured δ^{18}O [Bender, 2002, Battle et al., 2011].

2.3 The oxygen cycle

Molecular oxygen, O_2, currently constitutes around 21% of the atmosphere and is tightly bound to biological processes. In Table 2.1, the major constituents of dry air in today's atmosphere and the amount by volume are listed. The remaining fraction

is made up of various trace constituents such as neon, helium, methane and krypton. Oxygen has three stable isotopes; ^{16}O, ^{17}O and ^{18}O, whose abundances can be found in Table 2.2.

Molecule	% by volume
N_2	78.08
O_2	20.95
Ar	0.93
CO_2	0.0420

Table 2.1: Major constituents of dry air by volume.

Nuclide	Z	N	Natural abundance
^{16}O	8	8	0.99757
^{17}O	8	9	$3.8 \cdot 10^{-4}$
^{18}O	8	10	$2.05 \cdot 10^{-3}$

Table 2.2: Stable isotopes of oxygen.

Accounting for fractionation processes in the firn and ice makes it possible to estimate the isotopic ratio at the time of bubble close-off. However, to further assess what the isotopic compositions of oxygen reveal about the Earth's climate, understanding the fractionation processes inherent to the oxygen cycle is essential. In the following, the main climatic effects that can be inferred from $\delta^{18}O$ and $\delta^{17}O$ are presented as well as how $\delta^{18}O$ is used for relative dating of ice cores.

2.3.1 $\delta^{18}O$ and dating of ice cores

Oxygen in the atmosphere is created by photosynthesis in plants, a photochemical reaction where water and carbon dioxide are converted to oxygen and carbohydrates

$$6CO_2 + 12H_2O + \text{light} = C_6H_{12}O_6 + 6O_2 + 6H_2O. \tag{2.7}$$

No fractionation occurs during photosynthesis [Guy et al., 1993]. Thus, the isotopic composition of O_2 from photosynthesis reflects the isotopic composition of the substrate water, which is leaf water or seawater for terrestrial or marine plants, respectively. In figure 2.2, the main fluxes of the oxygen cycle are depicted, where processes associated with fractionation are denoted with the corresponding fractionation factor, α.

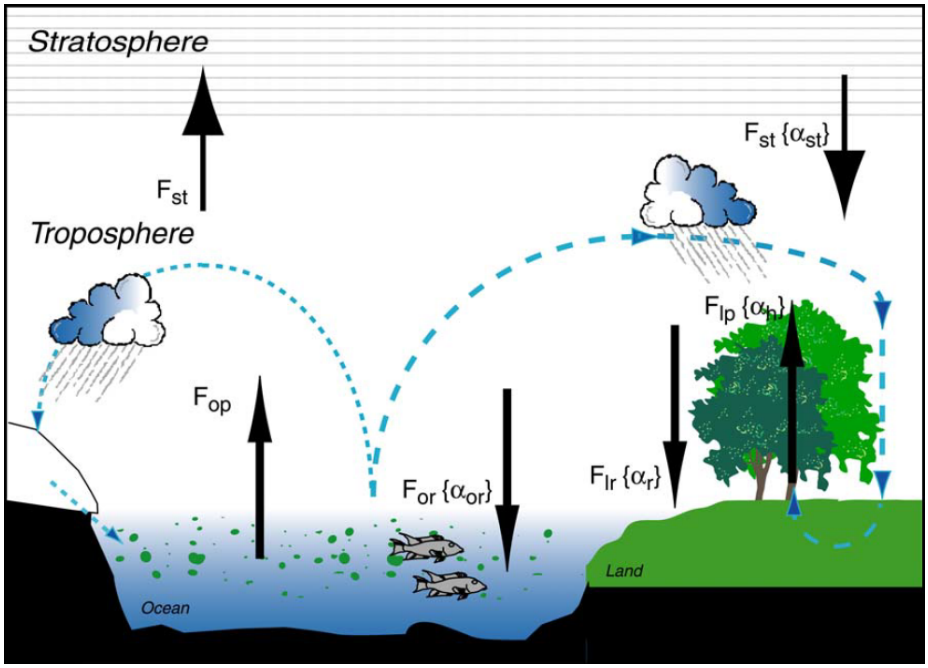

Figure 2.2: Main components of the oxygen cycle where F denotes the fluxes of oxygen and α is the fractionation factor for the respective process. Figure from T. Blunier.

Both aquatic and terrestrial plants respire, turning O_2 and carbohydrates produced by photosynthesis into energy. Respiration (F_{lr} and F_{or} in figure 2.2) serves as the primary sink of oxygen. This process preferentially removes lighter oxygen isotopes from the atmosphere,resulting in a positive $\delta^{18}O$ and $\delta^{17}O$ value of the atmosphere compared to the seawater. This anomaly is known as the Dole effect and has been estimated to be $(23.88 \pm 0.03)‰$ [Lane and Dole, 1956]. Respiration is an example of a mass dependent fractionation process which fractionates $\delta^{17}O$ about half of that of $\delta^{18}O$.

Steady state between photosynthesis and respiration is achieved when the amount of O_2 produced by photosynthesis equals that consumed by respiration. That is the case when $F_{op} + F_{lp} = F_{or} + F_{lr}$. In this scenario the atmospheric oxygen would yield a $\delta^{18}O$ of 18-20‰ relative to the standard mean ocean water (SMOW) [Blunier et al., 2002]. The higher measured value originates from a multitude of smaller corrections [Reutenauer, 2016], e.g. leaf water being enriched in $\delta^{18}O$ due to evapotranspiration [Dongmann et al., 1974]. This is also why the terrestrial photosynthetic flux of oxygen is associated with a fractionation factor, α_h, in figure 2.2.

Variations in $\delta^{18}O$ of leaf water and the ratio of land to ocean production are therefore tracable in the atmospheric $\delta^{18}O$. The production in turn is driven by changes of the meridional shift of the tropical rain belt correlating it with northern hemisphere summer insolation [Bender, 2002, Seltzer et al., 2017]. From its measured value the 23 000 year precession cycle of the Earth can therefore be inferred.

Interpreting high resolution climate records gives insight to detailed climate events.

To understand the succession of these events, being able to correctly determine their age is vital. Information is often inferred from ice cores from both hemispheres, and these must be coupled correctly to reach accurate conclusions on climate dynamics.

Most climate archives lack markers absolute dating. Therefore it is useful to date ice cores relatively to each other. All gases that have a global signal can in theory be used for synchronizing ice cores. The residence time of the gas in the atmosphere must be longer than its mixing time to ensure a proper imprint on the opposite hemisphere than where the change originated from. It must also be possible to obtain reliable measurements of the gas on both hemispheres. δ^{18}O of oxygen in the atmosphere has previously been used for such relative dating [Bender et al., 1994a, Blunier and Brook, 2001]. Since oxygen mixes globally its residence time in the atmosphere makes it ideal for detecting millenial scale changes. δ^{18}O thus permits correlation of ice cores across the hemispheres. This enables the synchronization of ice cores from Greenland and Antarctica.

2.3.2 The triple oxygen isotope composition

Since ^{17}O is about five times less abundant than ^{18}O in the atmosphere, reliable measurements of δ^{17}O requires higher precision. The combination of δ^{17}O and δ^{18}O measurements is a powerful tool to understand paleoclimates.

If all fractionation processes in the oxygen cycle were mass dependent, measuring δ^{17}O would not give any additional information to measuring δ^{18}O. However, in the stratosphere, a fractionation process that is not solely mass dependent occurs which affects δ^{17}O more δ^{18}O [Luz et al., 1999]. Air mixes from the troposphere to the stratosphere. In the stratosphere a complex isotope exchange between O_2, O_3 and CO_2 occurs. This process leaves δ^{17}O depleted compared to δ^{18}O, and mixes down to the troposphere, passing on the so-called anomaly. The fact that there is a mass independent fractionation process happening, makes it possible to separate the fractionation due to respiration from photosynthesis.

Therefore, it has been proposed that changes of δ^{17}O can be used to obtain the strength of photosynthesis in the biosphere [Blunier et al., 2002, Luz et al., 1999]. This makes the deviation a proxy for biologic productivity.

The triple isotope composition is defined as

$$^{17}\Delta \equiv \ln(\delta^{17}\mathrm{O} + 1) - \lambda_{ref} \cdot \ln(\delta^{18}\mathrm{O} + 1), \tag{2.8}$$

where λ_{ref} is a coefficient accounting for the exact ratio $\mathrm{O}^{17}/\mathrm{O}^{18}$ during fractionation processes influencing the modern air composition. Previous studies have shown λ_{ref} to be 0.518 [Luz and Barkan, 2005, Helman et al., 2005].

The measured $^{17}\Delta$ must further be evaluated by at the least a simple box model [Blunier et al., 2012] to infer biological productivity. This should account for several

mechanisms that influence the fractionation of stratospheric exchange and plant respiration. The strength of the stratospheric exchange is for example coupled to the amount of CO_2 in the atmosphere. Thus, to get a meaningful model one must include measurements of past variations of the CO_2 level in the atmosphere. It should be noted that $^{17}\Delta$ is a measure of biological productivity, however it gives limited information on the individually contributing processes.

Changes in biological productivity affect the climate in multiple ways. As terrestrial biomass increases, the atmospheric CO_2 concentration is lowered due to a higher amount of photosynthesis. The ocean biomass also promotes the effect of lowering the CO_2 concentration in the atmosphere. As more biomass is produced in the ocean and is transported to greater depths, the partial pressure of CO_2 in the surface ocean is lowered. This in turn lowers the concentration in the atmosphere as it reaches an equilibrium with the surface ocean. A lower CO_2 concentration promotes colder temperatures. However, increased vegetation in the terrestrial biosphere decreases the albedo of the Earth, which in turn increases the absorption of sunlight and thus the temperature.

2.4 Background on ice core samples

Most ice cores are drilled close to ice divides. The slow or negligible horizontal flow ensures that the deeper ice is originating from the same location on the surface. In this project samples from different ice cores have been measured for varying purposes, though they all stem from Greenland. In figure 2.3, a map of Greenland is shown where drilling sites are depicted with red markers.

Samples containing gas from the late Holocene have been measured as so called "test ice" as the $\delta^{18}O$ and $\delta^{15}N$ of these are well constrained. Except for firn processes, $\delta^{18}O$ resembles today's atmosphere due to the 1000 years residence time of oxygen and 10^7 years residence time of N_2. The test ice comes from the NEEM shallow ice core [Dahl-Jensen et al., 2013]. These measurements are valuable for gauging the precision, accuracy and continuity of the experimental setup.

At the end of the thesis work, samples from the RECAP ice core [Simonsen et al., 2019] were measured for the purpose of synchronizing the core with Southern hemisphere cores. The RECAP core is retrieved from the Renland ice cap in Eastern Greenland. Being so close to the sea, the Renland ice cap is strongly influenced by the change of Arctic sea ice export and Northern ocean currents.

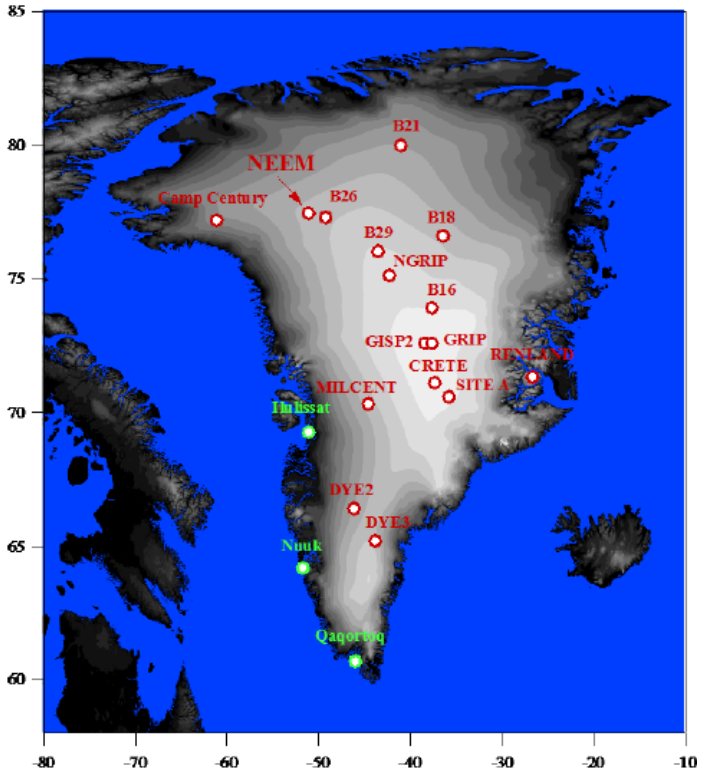

Figure 2.3: Map of Greenland where drilling sites are marked with red. The shading from gray to white indicates elevation. Figure taken from [Masson-Delmotte et al., 2015].

Ice core	Drilling period	Coordinates
RECAP	2014-2016	71.30°N, 26.72°W
NEEM	2009-2012	77.45°N, 51.06°W

Table 2.3: Name, drilling period and coordinates for the ice cores whose samples have been measured in the course of this project.

3 | Mass spectrometry

Mass spectrometry is a widely used method in many fields of science. In physics it is typically applied for isotope analysis. In very brief terms, a mass spectrometer (MS) ionizes the atoms and molecules of gas compounds and is able to separate and measure the amount of these by exploiting their difference in mass-to-charge ratio.

The first instrument to separate ions by their mass-to-charge ratio was constructed by J. J. Thompson in 1987, who is credited with the discovery of the electron. His work led to the discovery of atoms, isotopes and him being recognized as the father of mass spectrometry [Gross and Poole, 2018]. The technology has of course developed greatly in the 100 years since then and for this work a Delta V Plus Isotope Ratio MS from Thermo Fisher Scientific has been used. The work and alterations made to the MS are discussed in chapter 5. In this chapter, the underlying theory behind mass spectrometry is discussed and the concepts of a dual inlet MS systems are presented.

3.1 Concepts of mass spectrometry

As a gas is introduced to the MS, it first passes through a high vacuum ($\sim 10^{-8}$ mBar) ionization chamber where the particles are bombarded with electrons produced by a heated tungsten filament. A schematic of the process is seen in figure 3.1. This ionizes the molecules and atoms. Here one must be aware that there is a statistical chance that the electrons break molecular bindings, making recombination of molecules possible.

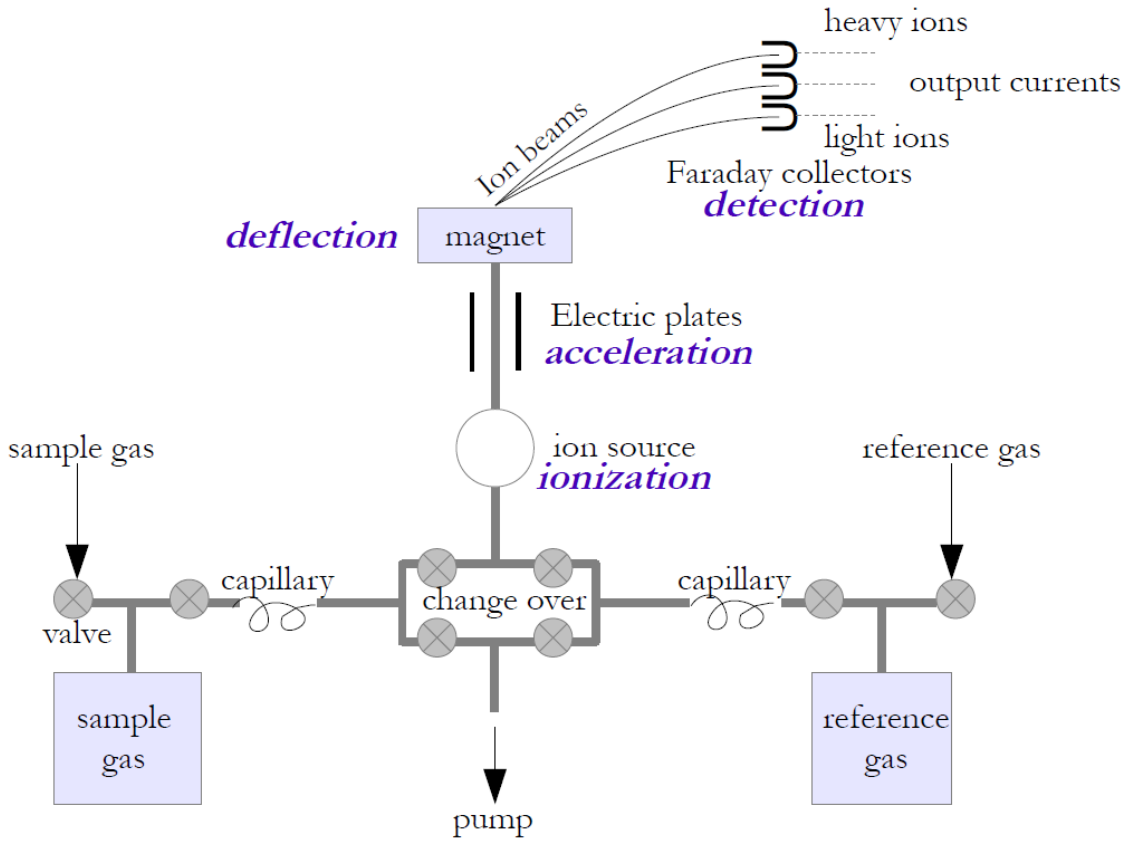

Figure 3.1: Schematic of processes in a dual inlet mass spectrometer. Figure taken from [Guillevic, 2013].

The ionized molecules are accelerated by passing through a voltage difference that creates an electric field. Then the compound is subjected to the electromagnetic field of a magnet perpendicular to the particle velocity. This separates the trajectories of molecules of different masses aiming at separate collectors. The force on a charged particle in vacuum due to electromagnetic forces is described by the Lorentz force law as

$$\mathbf{F} = q(\mathbf{E} + \mathbf{v} \times \mathbf{B}), \tag{3.1}$$

where $\mathbf{F}$ is the force applied on the ion, q its charge, $\mathbf{E}$ the electric field and $\mathbf{v} \times \mathbf{B}$ the vector cross product of the ion velocity and the magnetic field. Newton's second law of motion for the non-relativistic case is

$$\mathbf{F} = m\mathbf{a}, \tag{3.2}$$

where m is the mass of the moving body and $\mathbf{a}$ its acceleration. Equating the two expressions for the force yields the differential equation governing the motion of charged particles as

$$(m/q)\mathbf{a} = \mathbf{E} + \mathbf{v} \times \mathbf{B}. \tag{3.3}$$

Thus, by subjecting a group of ions to the same electromagnetic forces, their trajectories will be determined by m/q. The magnet in the MS deflects the ions on basis of this mass-to-charge ratio, commonly denoted as (m/z) where z is the number of elementary charges of the ion. The mass-to-charge ratio is typically noted as a dimensionless number describing the ratio of the mass number to the charge number of the ion. The ions are usually only ionized to have one extra electron. In table 3.1, the m/z referred in this work are listed alongside their molecules.

Chemical formula	m/z	Chemical formula	m/z
$^{14}N^{14}N$	28	$^{16}O^{18}O$	34
$^{14}N^{15}N$	29	^{36}Ar	36
$^{15}N^{15}N$	30	^{40}Ar	40
$^{16}O^{16}O$	32	CO_2	44
$^{16}O^{17}O$	33	N_2O	44
$^{17}O^{17}O$	34	H_2O	18

Table 3.1: Molecules and atoms that are measured and mentioned in this work alongside their mass-to-charge ratio for $z = 1$.

After being deflected, the separated ions hit Faraday cups. The ions are neutralized due to an electric current connected from ground to the cup. The cup then gains an electric charge. The ion current is integrated over a certain time interval and translated into a voltage signal using a resistor of high electrical resistance. The voltage intensities measured by the MS can then be directly translated to the relative amount of different m/z in the gas. Notice that the collectors have no way of distinguishing on other terms than this ratio, making e.g. CO_2 and N_2O ($m/z = 44$) or ^{17}O-^{17}O and ^{16}O-^{18}O ($m/z = 34$) fall into the same cup. This effect is known as isobaric interference.

The Delta V MS is equipped with a total of seven cups with widths of either 3.5 mm or 5.5 mm. Multiple collectors in the MS make it possible to measure several isotopologues simultaneously. For a certain strength of the magnetic field, these cups will measure a set of m/z of the ionized gas which is commonly called a cup configuration. In figure 3.2 a schematic of the arrangement and widths of the Faraday cups are presented. The figure also shows which configurations are used in this work, and how these assign m/z for the relevant cups. The $N_2/O_2/Ar$ configuration is utilized to measure $\delta^{18}O$, $\delta^{17}O$, $\delta O_2/N_2$ and $\delta^{36}Ar$. The N_2 configuration is used to measure $\delta^{15}N$. The CO_2 configuration is mainly used for verifying effects in the MS by measuring the isotopologues of pure CO_2.

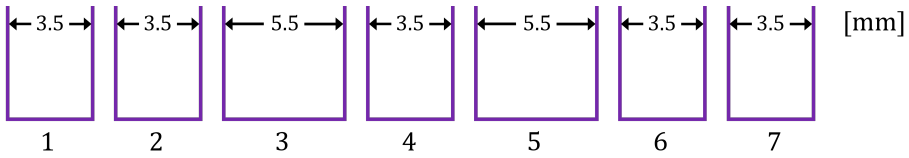

Configuration							
$N_2/O_2/Ar$	28	32	33	34	36	40	[m/z]
N_2		28	29	30			[m/z]
CO_2		44	45	46			[m/z]

Figure 3.2: Schematic of Faraday cups in the Delta V MS and the configurations used in this work. For each configuration, the m/z measured by each cup is shown.

In this thesis a method called "peak jumping" is also utilized. This refers to when a change in the magnetic field is made to deflect a different set of masses to the Faraday cups. This is a useful tool i.e. when measuring elemental ratios of masses too far apart to be a part of the same cup configuration. Previous work on the system [Grzymala-Lubanski, 2015, Reutenauer, 2016] was performed with another MS with fewer cups. Therefore, peak jumping was used more extensively. Changing between configurations is technically a version of peak jumping, but one usually refers to peak jumping when measuring one specific mass and not a range of masses which is the case with changing configurations.

3.2 Dual inlet mass spectrometry

As previously discussed, stable isotopic ratios are evaluated against a reference gas - typically a clean sample of current air. The precision on the resulting isotopic ratios is increased as sample signals are compared to the reference gas signals repeatedly. To be able to measure both sample and reference gases as frequently as possible in a similar way, a dual inlet (DI) mass spectrometer has been used. A schematic of a DI system is shown in figure 3.1. Sample and standard are injected into containers with adjustable volumes called bellows. For our experiment the left bellow (LB) contains the sample and the right bellow (RB) contains the reference gas. Varying the volume permits the user to change the pressure in the bellow. Gas flows from the bellow to the changeover block by a capillary. The capillaries constrict the flow. The changeover block consists of four valves. This unit allows admitting sample and reference gases sequentially into the ion source. The pressure in the bellows are adjusted so that the signal intensity is as similar as possible for the sample and standard.

It is important that an uninterrupted continuous gas flow is given for both capillaries. Fractionation can happen both in the capillaries and in the bellows. Keeping the system as symmetrical as possible limits these effects. When the differences are small, the resulting measurements can be corrected using a pressure imbalance test as described later in section 6.2.

3.3 Resolution

The precision of a single measurements is determined by the conditions in the MS. The resolution of a mass spectrometer, R, is defined as the ratio of the ion mass, m, to the mass difference, Δm as

$$R = \frac{m}{\Delta m}. \tag{3.4}$$

Δm denotes the smallest mass difference for which m/z signals of the same intensity are still distinguishable [Gross and Poole, 2018]. The resolution depends on how broad the ion beam is and which cup the measurement is performed with. The Delta V MS typically has a resolution of 110, fulfilling the so-called 10 % valley mode. This means that two neighbouring peaks of masses will only overlap where the peak intensity has dropped to 10% [Thermo Electron Corporation, 2005].

Though the error on a certain measurement can be small, the internal precision of the MS might be large if the same measurement repeated several times gives varying result. To fully evaluate this reproducability, analysis on zero-enrichment tests over time is presented in section 6.1.

4 | Experimental setup

A setup for extracting air occluded in bubbles of ice, as well as preparing and collecting gas for measurement of $\delta^{18}O$ and $\delta^{17}O$ is described in this chapter. First, the part of the setup able to measure $\delta^{18}O$ is discussed in detail. This section is also needed for measuring $\delta^{17}O$ and $\delta^{18}O$, but to successfully measure $\delta^{17}O$ an additional separation part must be included in the setup. This section is presented in the end of the chapter.

The setup consists of

- An extraction system
- A vacuum system
- A water removal section
- A CO_2 removal section
- A N_2 removal section for $\delta^{17}O$ measurements
- A collection unit

The function of every component of the line is explained along with improvements and adjustments that have been made to the original design of the setup [Reutenauer, 2016].

4.1 Requirements of setup

The gas sample introduced to the MS must be representative of the gas extracted from the ice core. Fractionation may occur as a result of e.g. temperature fluctuations and adsorption processes in the line. As it is near impossible to build a setup where no fractionation is present, it is rather aimed at treating the reference and sample in as similar ways as possible. This follows the principle of identical treatment [Werner and Brand, 2001]. The idea is that as long as the reference and sample are processed in a similar way, artifacts of the setup will cancel out as they are measured against each other.

The analytical precision required by an experimental setup depends on how small the expected changes of the δ-value are. A part of this thesis work is to verify a local maxima in δ^{18}O of the RECAP ice core at around 100 - 120 ky BP. In this interval δ^{18}O varies between -0.2-0.6‰. The measurement will be used to better constrain the time scale created for the RECAP ice core [Simonsen et al., 2019]. Due to its large variability, an external precision of 0.05‰will be sufficient to acquire data useful for establishing a time scale for the ice core.

To obtain meaningful measurements of δ^{17}O, one must be able to see variations as small 10 permeg (0.01‰) corresponding to its millenial scale variations measured in other studies [Blunier et al., 2002, Landais et al., 2007].

4.2 General layout for δ^{18}O measurements

A schematic of the experimental line used for extraction of gases in ice cores, removal of water and CO_2, and collection of the gas can be seen in figure 4.1. This configuration of the setup is meant for δ^{18}O measurements and has bypassed an extra separation part needed for δ^{17}O measurements between valves L2 and L7.

During extraction, ice samples of $\simeq$ 40 g are enclosed in extraction vessels. The vessel is connected to one of the valves E1-E10 as seen in figure 4.1. The vessel is evacuated with both a rough pump and a turbomolecular pump through valve P1 for 10 minutes to remove any atmospheric air that has diffused into the outer layer of the ice sample after cutting. Meanwhile the vessel is submerged in a cold bath consisting of ethanol at (-45 ± 5)°C.

The cold bath is switched out with a warm bath consisting of water kept at $(+45 \pm 1)$°C. This melts the ice and releases gas enclosed in bubbles in the ice. At the same time the pathway from the extraction vessel to one of the dip tubes, or rods, is free (R1-R10). The collector dip tubes are kept at cryogenic temperatures ($\simeq$10-12 K). This creates a local pressure gradient that pulls the gases from the ice samples through the line to be trapped and solidified in the dip tube.

The gas is first subjected to water traps (T1 and T2) kept between -80°C to -100°C. These traps capture any water vapor that is carried with the gas from the extraction vessel. Due to the presence of water in this section of the setup it is termed the "wet part".

After water is removed from the sample, the gas moves through a CO_2 trap, T3, which traps CO_2 by freeezing it at -196°C. This is achieved by submerging the trap in liquid nitrogen (LN_2). The section of the setup from trap T3 to the dip tube should at no time contain water in any form. Therefore it is called the "dry part".

Now the gas contains neither water nor CO_2, but is mainly a mixture of N_2, O_2 and Ar that has been preserved in bubbles of ice. This gas is trapped in the dip tube and solidifies due to the low temperature. After all extractions on a certain day are finished, the dip tube is heated up again. The solid mixture becomes gaseous and is

allowed to diffuse within the dip tube. The next day, the gases are introduced to the sample bellow of the dual inlet system in the MS to be measured.

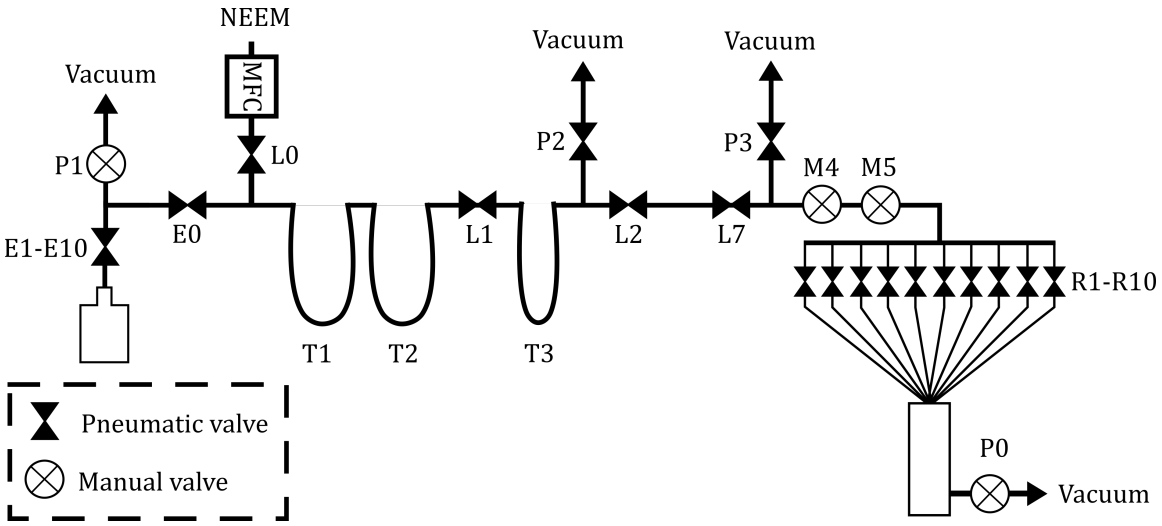

Figure 4.1: Schematic of the experimental setup for $\delta^{18}O$ measurements where the N_2 separation part is excluded. Valves P0-P3 lead to the vacuum system described in figure 4.2.

4.3 Vacuum system

Although technically not part of the sample line, a robust vacuum line is critical in any gas measurement system. A detailed schematic of the vacuum system can be found in figure 4.2. It consists of a low vacuum (LV) rough pump (Duo 2.5, Pfeiffer) and high vacuum (HV) turbomolecular pumping station (HiCube, Pfeiffer) connected to the same volume. The pressures in the setup are monitored by pressure gauges (Pirani, Edwards). From the vacuum system, valves P1-P3 lead to the line, while the manual valve P0 connects the LV pump to the vaccum casing of the collection manifold. This allows for the different parts of the setup to be evacuated and brought to vacuum at different times. To protect the turbo molecular pump, it is only opened to the line after the oil pump already has reached a pressure below ~ 0.1 mBar.

The dip tubes are encased in a vacuum casing. By evacuating the casing to vacuum, the empty space serves as insulation and is necessary for reaching cryogenic temperatures. The vacuum casing is evacuated only with the LV pump by closing the pneumatic valve, PL, between the HV and LV pumps. The casing must be evacuated separately from the line because it contains vacuum grease which poses a possible contamination of the line.

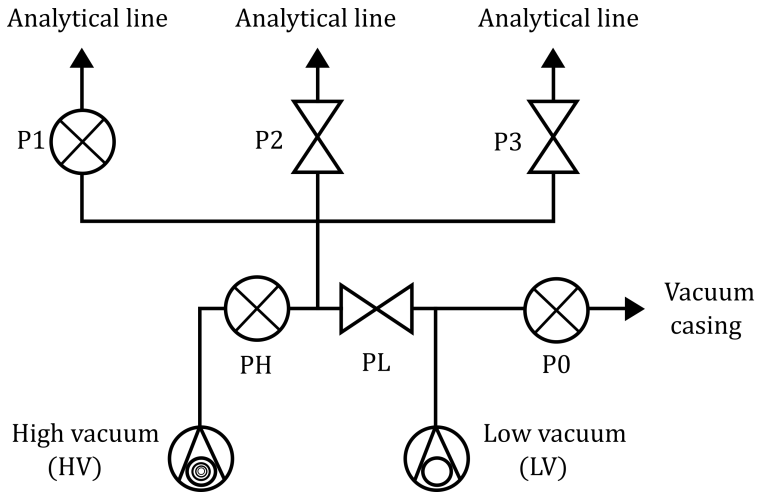

Figure 4.2: Detailed schematic of pump system where P0 and P1 are manual valves and P2, P3 and P4 are pneumatic valves.

In addition, after every ice sample is extracted and collected, the "wet part" of the line is evacuated by the rough pump keeping only P1 and PL valves open. This is to protect the turbomolecular pump and the dry part of the setup from water vapor. This vacuum system has proved efficient and its simplicity makes it reliable to work with.

4.4 Sample preparation

Samples of ice are cut by an electric band saw inside a cold room. It was found that samples should be around 40 g to yield 4 cc of gas, which is the amount of gas the setup is designed for [Reutenauer, 2016].

Great care is taken to avoid possible contamination of the sample. All samples are handled with clean gloves. Any visible cracks are cut away from the sample as illustrated by the red line in figure 4.3. The example in the picture is one of the samples from the RECAP ice core. Here only the part below the red line was used for extraction.

Samples used for gas analysis typically have a curved side as seen to the left of the sample in figure 4.3. This curved side has a greater chance of being contaminated by drill fluid and of suffering from post coring gas loss. Therefore, at least 0.5 cm of this part is cut from the sample.

After the sample is cut to $\simeq$40 g, all sides are shaved with a ceramic knife further removing $\simeq$2 mm of all surfaces. The final weight of the sample is noted.

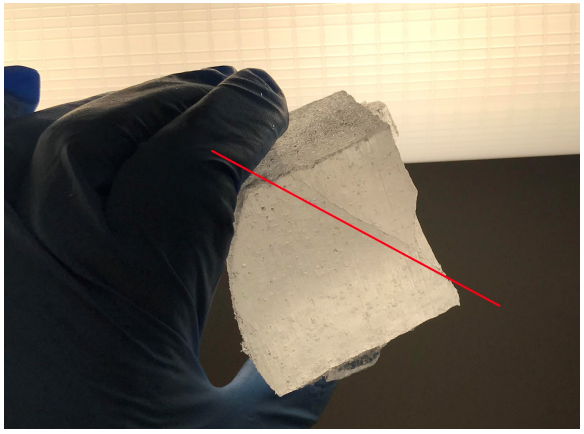

Figure 4.3: Picture of a RECAP sample that was cut at the illustrated red line to avoid contamination stemming from the visible crack in the ice.

4.5 Extraction system

After cutting and shaving the sample, it is enclosed in an extraction vessel (figure 4.4). The upper part of the vessel is a 6 mm glass tube that can be connected to one of the valves E1-E10 with a SWAGELOK 1/4" Ultra-Torr fitting with a viton O-ring.

The gases occluded in bubbles in ice samples are retrieved by a melt-extraction technique. This is a common method for extracting gases such as O_2 and N_2. Other gases require so-called dry extraction methods, such as crushing the ice to extract the gases. This is e.g. the case for CO_2 which due to its high solubility in water, will not yield precise measurements if extracted with a melt-extraction technique [Sowers et al., 1997].

Figure 4.4: Photograph of glass extraction vessels along with their O-rings and connectors. Figure from Grzymala-Lubanski [2015].

Before melting, the vessel containing the sample is submerged in pre-cooled ethanol between -45°C and -55 °C. The vessel containing the sample is evacuated by the LV and HV pump for 10 minutes. Then the cold bath is switched out with a warm bath consisting of water kept at (45 ± 1)°C. This typically results in a melt time between 5 and 7 minutes, depending on the size and density of the ice sample.

The setup can accommodate ten extraction vessels. The samples are introduced one by one through the line, with a minimum of 30 minutes intervals due to evacuations of the line and transfer time. This is to avoid cross contamination of the samples. Leaving the samples for different times in the sample flasks can be a source of additional uncertainty. A procedure for cutting and keeping several samples cold at once was therefore not developed. Instead every sample was cut and shaved immediately prior to extraction, and inlet E2 was used for every ice sample in this project.

Some tests have been conducted in the system by using dry reference gas. In these cases the gas is introduced through the mass flow controller (MFC) on the upstream side of valve L0.

4.6 Water removal

As the ice samples are melted, water vapor is typically carried along with the released gases. This water vapor has to be removed from the air sample to prevent potential isotopic exchange with atmospheric oxygen. Therefore, the gas compound is subjected to two water traps, T1 and T2. These are cylindrical stainless steel (SST) tubes filled with glass beads (2 mm outer diameter) to allow for a large surface area where the water vapor may freeze on to.

The traps are submerged in a mixture of ethanol, LN_2 and dry ice kept between -100°C and -80°C. Since the system operates in the mBar range, the traps need to be sufficiently cold to ensure freezing. However, were the water traps to be submerged into even colder baths (such as pure LN_2), fractionation may occur due to O_2 and N_2 freezing to the water at this temperature. For this reason the water traps are placed before the CO_2 trap, which is submerged in LN_2, in the setup.

Development of the water traps

The original design of the water separation unit consisted of only the T2 trap (see figure 4.5). On the upstream side a flow restriction of 1/16" SST tubing ensured that the trap would not be clogged by freezing water at the entrance. Trap T2 has an inefficient design. During previous work on the system, it was evident that a trap with larger capacity was needed. The SST cylinder of T2 was therefore extended to be 8 cm longer than the bottom of the inner tubing. In addition, it is turned the opposite direction than what is customary, as one would normally want the gas to flow through the beads before being forced into the smaller volume (1/4" SST tubing). Hence, this trap creates dead volume that is not utilized for freezing the

water vapor.

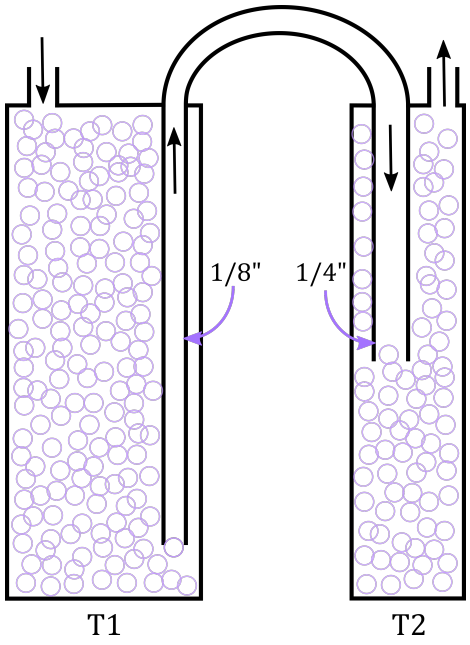

Figure 4.5: Detailed schematic of the two water traps. Arrows indicate the direction of gas flow and the glass beads are shown by purple circles.

Tests were made both with dry gas and gas extracted from recent Holocene NEEM ice samples (see sections 7.1 and 7.3). In brief, comparison of standard deviations between the NEEM test samples (wet samples) and standard gas in the rods (dry samples) suggests that the presence of water vapor in the samples might increase the measurement uncertainty. This lead to a discussion on whether water vapor might be causing additional uncertainties. If not all water vapor would be removed by the trap T2, it may freeze in the CO_2 trap, T3, which is kept at LN_2 temperature. This might lead to fractionation of the samples due to incomplete cryotrapping at the collection manifold.

To rule out that any water vapor is left after the trap, a second water trap was added. This is T1 as seen to the left in figure 4.5. The gas is allowed to flow through the beads before entering a 1/8" SST tubing at the bottom of the cylinder. Though the SST tubing is narrower than that of T2, the trap itself has a larger volume and therefore a larger surface area and capacity for freezing out the water vapor than T2.

As the second water trap was added, it became evident that the restriction on the upstream side of the water traps was not necessary. Though more water vapor enters the traps, the transfer is more efficient and no freezing of water is seen in T2. With these two water traps, one can be confident that the water removal of the system is reliable and complete. In figure 4.6, T1 is shown after the introduction of two samples to the system and removal of non-frozen beads. The water trap clearly has much more capacity and little to no frozen water is seen at the bottom of the trap where the temperature tends to be colder. This indicates that all the water is frozen

out efficiently at the top of the trap.

Figure 4.6: Inside of water trap, T1, after two samples have been melted and extracted. Water vapour freezes the glass beads along the walls.

4.7 CO_2 removal

In section 3.1 it was discussed how the MS cannot distinguish between molecules of equal m/z values.

To avoid the kind of isobaric interference discussed in section 3.1, CO_2 needs to be removed from the measured gas. In addition to this, the gas chromatography column in the N_2 separation part tends to trap CO_2, making it important that CO_2 is trapped before the gas enters the additional separation unit needed for $\delta^{17}O$ measurements.

The CO_2 trap is a SST 1/8" outer diameter "U"-shaped trap submerged in LN_2 (-196°C). As the boiling point for CO_2 at atmospheric pressure is -78.45°C, it is certain that the CO_2 freezes to the walls even at lower pressures in the operating system. Between every extraction the CO_2 dewar containing LN_2 is lowered and the trap heated up by a household type hairdryer to avoid clogging.

4.8 Collection unit

A detailed description of the collection unit and its design is given in [Reutenauer, 2016]. In this section, a brief overview will be provided along with some adjustments made to the original design. The collection unit consists of 10 dip tubes which are 1/4" SST tubing, each with a volume of $\simeq$9 ml. These are connected to the line with pneumatic valves. At the bottom of the dip tubes is a copper block connected to a He cryocooler cold station. The dip tubes and cold station are enclosed by a vacuum casing for insulation purposes. The vacuum casing is connected to the LV pump

(figure 4.2). As the cold head reached cryogenic temperatures, the temperature and pressure gradients drive the gas in the system to be collected and solidified in the dip tube open to the system.

4.8.1 Cryocooler and vacuum casing

The cryocooler is a closed cycle cooling system consisting of a compressor and a cold head. Helium is compressed and actively removes heat from the cold head by re-expanding. This makes it possible to cool the copper block to 10-12 K.

The vacuum casing needs to keep vacuum well. Major leaks poses a safety threat as most gases are solidified at 10-12 K. If the collection manifold is heated up while a large amount of gases have accumulated, the vacuum casing may burst. The vacuum in the casing was observed to rise from $\sim 10^{-2}$ mBar to $\sim 10^{-1}$ mBar over 24 hours. The temperature of the collection manifold at this time could only reach about 13 K. The O-ring on the top of the dip tubes connecting them to the vacuum casing was exchanged to one of a slightly larger outer diameter (2.8 mm to 3.0 mm). This alteration was observed to hold a low pressure much longer. In addition, it enabled the cryocooler to reach a temperature of 10-11 K. This in turn improved upon the trapping efficiency of the collection manifold.

4.8.2 Conditioning of dip tubes

To achieve a stable equilibrium between ad- and desorption processes on the SST surfaces of the dip tubes during sample collection, the dip tubes are conditioned at all time. Dry modern air where CO_2 has been removed is introduced to the rods at the same pressure as a sample would be (225 mBar to 450 mBar). When measurements are conducted every day, the rods are conditioned by the leftover sample gases from measurements the day before. If the dip tubes have been evacuated for a long time or contamination by e.g. CO_2 or water vapor is suspected, no measurements are made until the rods have been conditioned for at least 24 hours.

4.8.3 Passivation of dip tubes

Over time the SST tubes of the dip tubes consume O_2. Depending on the frequency of use for the dip tubes, it can be practical to passivate them occasionally. The passivation is done in order to create a permanent reaction between the SST surface and O_2 where the SST surface is saturated with O_2 and does not consume the gas of the sample. The passivation procedure developed at Scripps Institute of Oceanography is followed (R. Beaudette personal communication).

First, the dip tubes are filled at overpressure with pure O_2 (2-3 bar). Then the collection manifold is removed from its vacuum casing. A thermocouple is placed in the middle of the rods and connected to a PID controller.

To avoid uneven heating and direct heating on the outer surfaces of the dip tubes, the tubes are inserted in an aluminum cylinder meant to distribute the heat better. As seen in Figure 4.7, the inner diameter of the cylinder is smaller than the outer diameter of the upper copper block of the collection manifold. This is to avoid heating up and subsequently deforming the O-ring. However, this also means that only the lower part of the dip tubes are heated.

Heat tape whose input current is controlled by the PID is wrapped around the aluminum cylinder. To further stabilize temperature, aluminum foil is wrapped around the heat tape. The whole setup is seen in Figure 4.8. The PID is set to control the temperature to reach 145°C inside the collection manifold and left "baking" for 48 hours.

An alternate method to improve on the surface conditions of the rods might be to bake them at high temperatures as described, and evacuate the dip tubes at the same time. This would increase the probability of molecules being desorped from the surface. However, conditioning them rigorously is also expected to remove the effect of molecules adsorption at the surfaces.

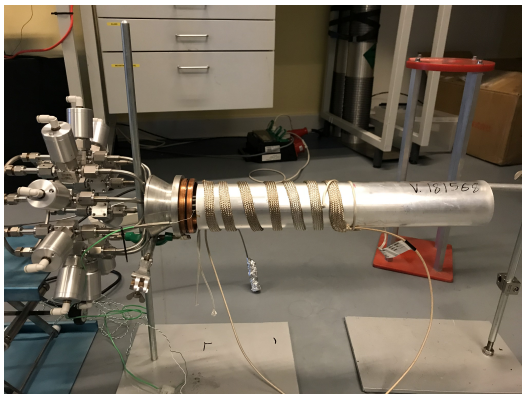

Figure 4.7: Picture from the baking of the dip tubes. Heat tape is shown to be wrapped around the aluminum cylinder.

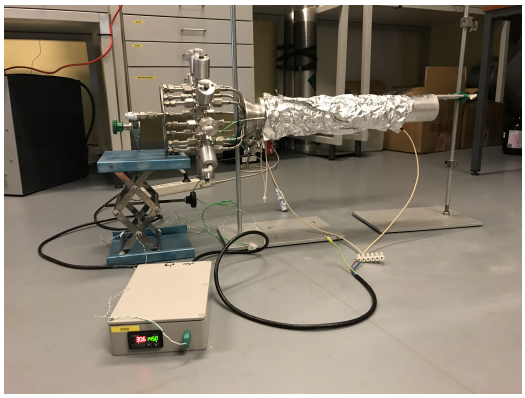

Figure 4.8: Picture of complete setup for baking the dip tubes.

4.9 General layout for $\delta^{17}O$ and $\delta^{18}O$ measurements

To measure both $\delta^{17}O$ and $\delta^{18}O$ of gases in ice cores, an additional separation step must be taken. In figure 4.9, the experimental setup including the N_2 separation part is shown.

This part consists of

- Two identical full air traps
- A gas chromatography (GC) column
- A thermal conductivity detector

During $\delta^{17}O$ measurements, the gas is trapped in the full air trap, T4, after CO_2 removal. This happens as the trap is submerged in LN_2. When all gas is trapped, V1 is closed to the left part of the line and the trap is heated up to room temperature. Ultrapure He is applied to the trap, carrying the captured gases to the GC column.

In the GC column, different gases are adsorbed for different amounts of time. O_2 and Ar are kept for a shorter time than N_2. This makes it possible to trap the O_2-Ar mixture in the full air trap T5 before using V3 to let N_2 out to waste instead of trapping it in T5. The trap T5 is then heated up and the remaining O_2-Ar mixture is trapped in a dip tube in the same way as for $\delta^{18}O$ measurements. The gas is measured the next day, but the reference gas will be pure O_2 instead of air as is the case for $\delta^{18}O$ measurements.

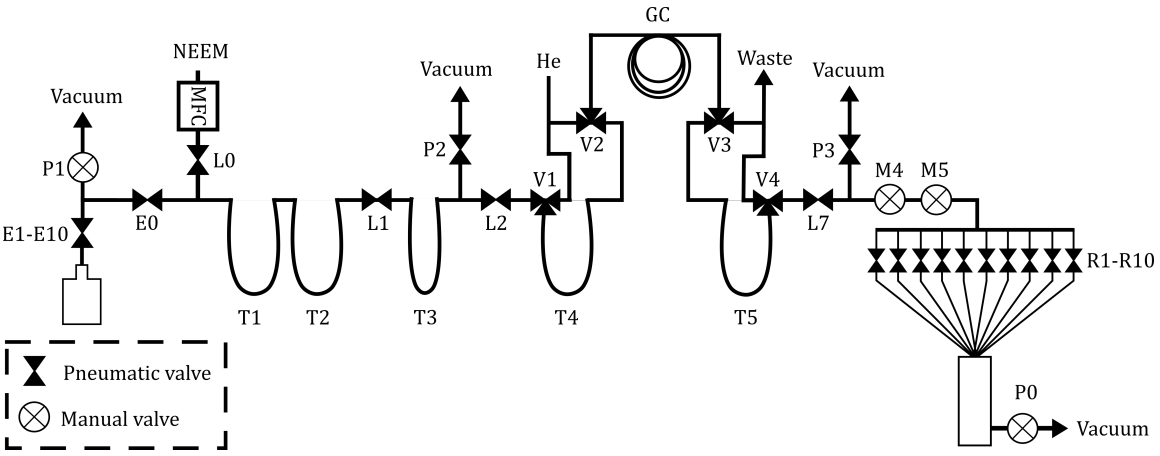

Figure 4.9: Schematic of the analytical system for triple oxygen collection. The setup consists of an extraction, purification separation and collection part.

4.10 N_2 removal

For measuring $^{17}\Delta$, N_2 must be separated from O_2-Ar in the gas to avoid formation of interfering masses in the ionization chamber of the MS. Typically N_2 and O_2 in the

source recombine to $^{14}N^{18}O$ which has $m/z = 32$ as $^{16}O^{18}O$ [Barkan and Luz, 2003].

For $\delta^{18}O$ measurement this part is bypassed by 1/8" SST tubing between valves L2 and L7. Though this part of the system has not been brought to a functional state yet, work was performed to create a stable temperature system for the GC. Therefore this section of the setup will also be briefly described with an emphasis on the temperature system of the GC.

4.10.1 Focusing traps

T4 and T5 are identically constructed focusing "U"-shaped traps. Both consist of $\simeq$ 40 cm long 1/4" SST tubing filled with molecular sieve material (5A, 30-40 mesh size). These are called focusing traps as they are intended to trap all gases allowing for the mixture to be released simultaneously. The full air trap T4 is submerged in LN_2 and the molecular sieve material captures the gases. When all gases are trapped, L2 is closed and T4 is heated up to room temperature. Then the gases are pushed out of the trap by high purity He ($\leq$ 99.999%) stream. The GC column will only successfully separate N_2 from O_2 and Ar if all gases enter approximately simultaneously. After N_2 is separated from O_2 and Ar as discussed in the following, T5 is used to capture the O_2-Ar mixture. The N_2 gas is flushed to waste and the He supply closed before T5 is heated up and the O_2-Ar mixture is collected by the collection manifold.

4.10.2 GC column

The separation of O_2-Ar from N_2 is carried out in the GC column (88014-800, Restek, USA). It is a 3 m long SST tubing with an inner diameter of 2 mm packed with molecular sieve material (5A, 80-100 mesh size).

As the gas is pushed by the He carrier gas through the GC, molecules of different gases are trapped at varying time intervals. GC columns are made in a variety of lengths and materials, typically making it a unique challenge to optimize the separation. The adsorption time depends on the temperature of the GC column and the velocity of the carrier gas.

The goal of the GC system is to separate N_2 from the O_2-Ar mixture and so that N_2 is let out to waste, while O_2-Ar is captured in the focusing trap, T5. Knowing the peak separation and timing of the peaks is therefore vital to achieve this.

The separation can be assessed by the output of a thermal conductivity detector (TCD) on the downstream side of the GC. The TCD measures the difference in thermal conductivity between the sample flow from the GC column and the carrier gas flow (He). Thus it will show a spike in intensity when a gas passes through. In figure 4.10, an illustration of the intensity of gases passing through a TCD is shown. A higher temperature results in a narrower gas peak, but poorer separation of the gases. This relationship has to be empirically derived.

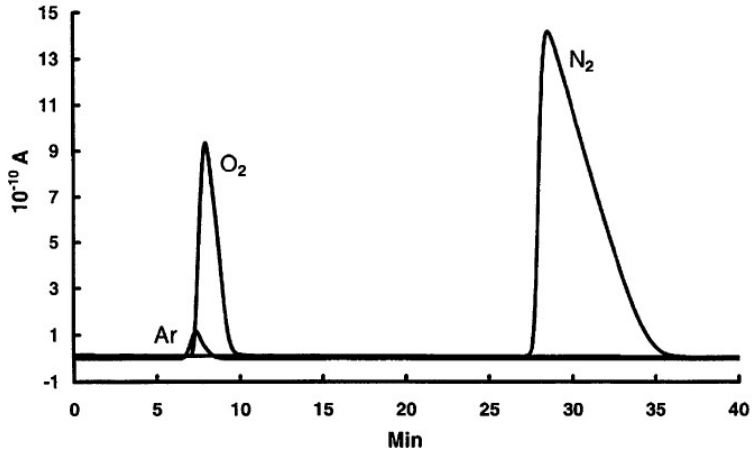

Figure 4.10: Figure 2 from Barkan and Luz [2003], original caption: Chromatogram showing separation of N_2 from O_2-Ar mixture. He flow rate is $\simeq 25$ mL·min^{-1}.

4.10.3 Original temperature system

To determine the timing of peak separation, it is essential that the GC column is kept at a stable temperature over the time of separation. The original temperature stabilization system consisted of an insulated box with a peltier element and an LN_2 pump. Both the power supplied to the peltier element and to the LN_2 pump were controlled by separate PID (proportional–integral–derivative) controllers with a set point at 0°C.

The peltier element by itself was not powerful enough to cool the temperature down to 0°C with a maximum cooling capacity at about 6°C. Its PID controller was in addition not able to keep a stable temperature. When testing a set point the peltier element is powerful enough to reach (e.g. 15°C), the temperature would still oscillate with ± 4°C.

The LN_2 pump consists of a dewar filled with LN_2, a funnel with an electrical resistor (10 Ω) leading to a plastic tubing pumping the LN_2 to the GC box. When a current flows through the electric resistor, electrical energy is converted into thermal energy. Due to the Leidenfrost principle, a steep temperature gradient is created in the funnel, and droplets of LN_2 are levitating on N_2 vapor up by an insulated layer of N_2 [Linke et al., 2006]. This transfers LN_2 to the GC box.

The LN_2 pump by itself was not able to keep a stable temperature of around 0°C, but overshot with several °C. The LN_2 pump was observed to quickly consume LN_2. This decreases the pressure in the funnel and thus the power of the pump. To counteract this, the LN_2 reservoir volume was increased to minimize LN_2 loss and thus the pressure decrease in the dewar. The dewar was topped up every 10 minutes to keep a constant pressure. A fritted filter was added to the outlet side of the plastic tube for better distribution. This decreased the overshoot of temperature somewhat.

Despite these efforts, the most stable configuration that was achieved had a temper-

ature varying ±1.5°C from the temperature set point with a period of approximately 5 min. This was deemed to be unacceptable for the GC column, and a new temperature stabilization system was designed.

4.10.4 A new temperature stabilization system

The new temperature stabilization system does not rely on any consumables, only on electrical components. The GC column is wrapped with a PID-controlled heating tape and isolated with pipe foam insulation. This is placed inside a small household freezer (Wasco f31w). A picture of the system is shown in figure 4.11. The freezer temperature varies between -25.5°C to -22.5 °C. The cooling provided by the freezer is counterheated by the heat tape to achieve a temperature of 0°C. The temperature is monitored by a k-type thermocouple placed between the insulation material and the heat tape. The thermocouple is connected to a PID to keep the temperature stable.

Figure 4.11: Picture of isolated GC column inside the freezer. The connection to the power supply for the heat tape is achieved by fitting the wires through holes drilled through the ceiling of the freezer.

The resistance, R, of the heating tape is 186 $\Omega \cdot \mathrm{m}^{-1}$. It was found that a voltage, U, of (37 ± 1) V applied to the heating tape was sufficient to counterheat the freezer temperature to 0°C at its coldest cycles. The total power, P, applied to the system is thus

$$\frac{U^2}{R} = P = 7.36 \text{ W}.$$

The system relies on a single PID controlling the heat tape, as opposed to the previous two of the original system. The autotuning function of the PID resulted in unacceptable temperature overshooting. Therefore, the PID is instead tuned by the closed loop Ziegler/Nichols tuning method [Ziegler and Nichols, 1995] applied to our

system. The main idea of this method is to omit the derivative gain term in the PID equation, as it makes the problem too complex to solve in a reasonable amount of time. Applying the method successfully achieved a temperature of 0.0 ± 0.1°C, which is within the uncertainty on the PID's temperature measurement.

It should be noted that the k-type thermocouple typically has a systematic error of ± 2.2° C for the relevant temperature range. As the choice of temperature in the GC will need to be optimized empirically through reviewing chromatograms for different temperatures, this possible offset does not need to be taken into account.

4.11 Chemical CO_2 trap

Previous measurements with the system removed CO_2 from the sample but not from the reference. As will be discussed in detail in section 6.6, it was evident that CO_2 has a non-negligible impact on the measured $\delta^{18}O$, and a chemical CO_2 trap was therefore included for the reference gas to flow through before being introduced to the standard site of the dual inlet system.

The chemical CO_2 trap is a 1/4" SST tubing of 18.5 cm length. A schematic can be found in figure 4.12. In both ends of the tubing there 1.5 cm of glass wool to keep the line clean and prevent chemicals from diffusing out of the trap. On the upstream side there is about 10 cm of ascarite (sodium hydroxide coated Silica) and on the downstream side about 5 cm of magnesium perchlorate ($Mg(ClO_4)_2$). The ascarite removes CO_2 but creates some water in the process, which is absorbed by the magnesium perchlorate.

After some time the trap will saturate and have to be replaced. To monitor when this is necessary, it is recommended to continue to measure mass 44 by peak jumping regularly. Notice that for measurements of $\delta^{17}O$, the standard will be pure O_2 and the CO_2 trap will not be needed anymore.

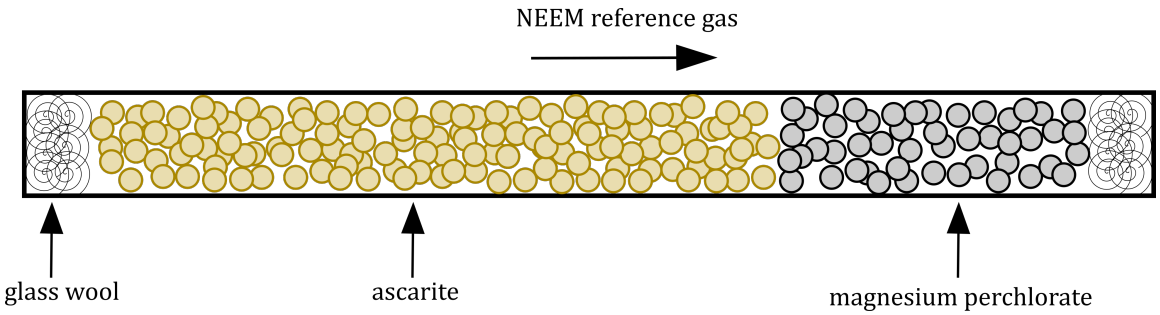

Figure 4.12: Schematic of the chemical CO_2 trap with the direction of NEEM reference gas flow denoted by an arrow.

4.12 Automation of setup

To achieve the same separation in the GC for every sample extraction and thus high comparability between measurements, automation of the setup is necessary. Most parts of the setup can be controlled remotely by a LabView virtual instrument with the exception of a few valves. Some valves opening to the collection manifold or the HV pump are deliberately manual so that a user can interfere if software problems occur or either the safety or functionality of the units are compromised.

The valve between the water trap and the CO_2 trap, T3, was switched from a manual valve to a pneumatically actuated valve, and a control made in our LabView virtual instrument.

Timing opening of a control

To begin the task of creating sequences in LabView for measurements, a timing function for the MFC was created. The MFC can now be controlled remotely to be open for a set amount of time. This makes it possible to flow the same sample amount every time a test with dry gas is performed.

The timing function was created by applying a so-called "state machine" in LabView as shown in Figure 4.13. The front panel is shown to the left and the block diagram is to the right. The front panel is the GUI that the user is seeing while operating the instrument, while the block diagram is the programming part where the visual code is written. The user is now able to set a time in the LabView environment in which the MFC will be open and flow gas to the line from the reference gas bottle.

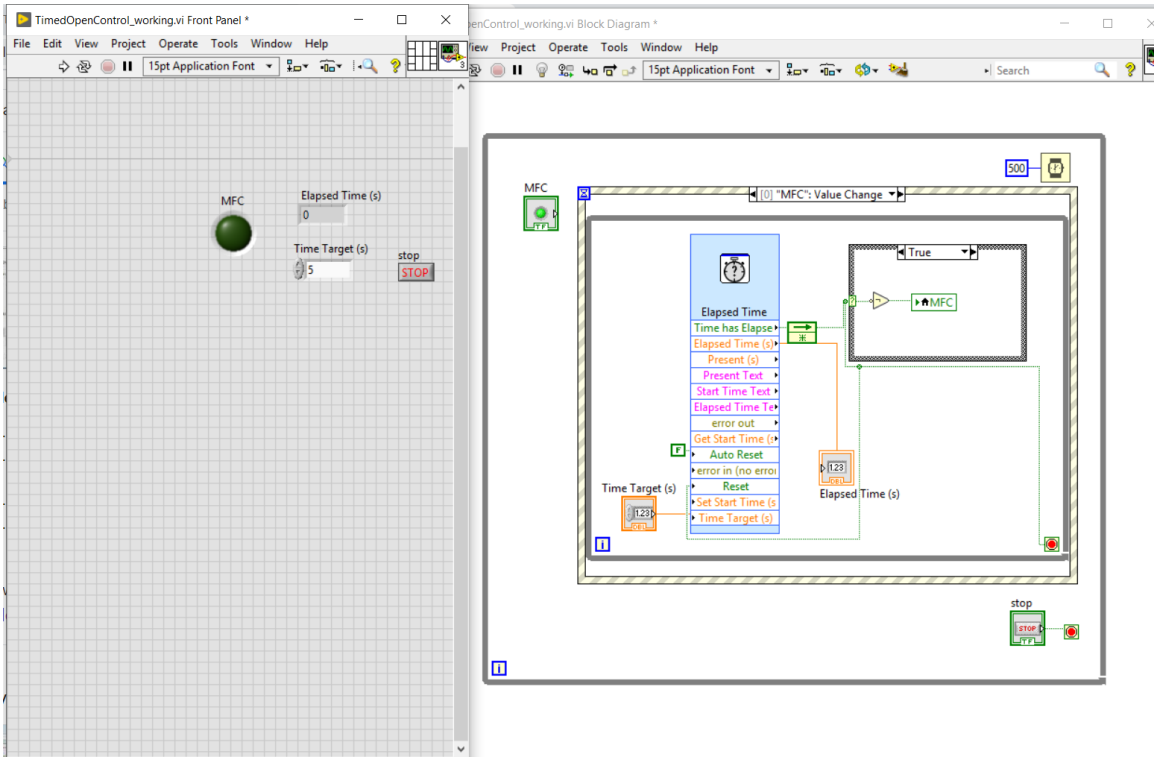

Figure 4.13: Example of visual code in LabView for timing the opening time of a control.

5 | The Delta V Plus MS

5.1 Isodat NT

The software provided by Thermo Fisher is called Isodat NT and allows the user to monitor conditions in the MS and optimize measurement procedures. To perform a measurement with the MS, one need so-called sequence files, method files and ISL scripts. An overview of the main functions of these files are given here.

In the *sequence file*, the user decides what type of measurement is performed by creating a set of rows that are executed sequentially. For every row it can be determined if the instrument should fill each bellow and where the gas should come from. In the case of the O_2 system this is either from a specific dip tube or from the reference gas line.

Every row of the sequence file calls upon a *method file*. In the method file the user determines:

- What cup configuration is used.
- How many cycles of measurements are performed.
- Delay time before the measurement cycles begin.
- Integration time for a single measurement.
- The target intensity measured on a certain cup, which is achieved by changing the bellow volume, and so change the flow to the MS.

The method files were edited to contain a possibility for automatic peak jumping during measurements. This now allows the user to peak jump with a certain cup to a set mass, perform a peak center and measure the certain m/z at the cup after the traditional measurement. This is useful for gauging whether there is H_2O present in a sample or monitor CO_2 levels in a reproducible way over time.

Every method file calls upon an *ISL script*. The Isodat NT Script Language (ISL) allows the user full access to the MS functions. For this work, custom ISL scripts were created to:

- Open both changeover valves from the bellows to the MS at the same time. This was useful for the chemical slope measurements where the contents of both bellows were mixed dynamically while introducing gas from both bellows to the MS at the same time.
- Change the "set bellow position" function. In the default settings the bellow position always increases to 100% before adjusting to the manual set position decided by the sequence. For the chemical slope procedures it was observed that rapid changes in the volume of the bellows caused fractionation similar to what is found by [Bereiter et al., 2018]. This is discussed in detail in section 6.3.

5.1.1 Measurement cycle in MS for δ^{18}O

For measuring δ^{18}O, two rows in the sequence file are dedicated to each sample. The first performs a measurement with the $N_2/O_2/Ar$ configuration and the next with the N_2 configuration. The RB and LB are both compressed to achieve a (7800 ± 50) mV signal on cup 4 ($m/z = 33$) for the $N_2/O_2/Ar$ configuration and to (8600 ± 50) mV for the N_2 configuration with the same cup ($m/z = 29$). Cup 4 is chosen because it is the most sensitive cup. The sample is measured against the reference over 16 cycles with a 16 seconds integration time for each cycle. The standard deviation of the measurement is determined and serves as a measure for uncertainty estimations.

5.2 Capillaries

5.2.1 Crimping of capillaries

For the pressure imbalance effect to be as small as possible, it is essential to obtain as similar flows from the two bellows into the MS as possible. The pressure imbalance correction is only linear for slight changes. It was observed that the flow from the two bellows is unequal by $\simeq 1000$ mV for the same pressure in the bellows ($\simeq 50$ mBar), hence redoing the crimp on the capillaries became necessary.

The crimping is performed manually by adjusting the screw on the crimping block of the capillary in question. It is impossible to "uncrimp" a capillary - once it has been deformed it cannot be widened again. Therefore, one capillary was slowly crimped meanwhile observing the measured voltage of a certain cup as the flow switched between the LB and RB. To ensure that the pressures in the bellows are actually the same, the outer valves of the bellows were open to the same volume while flowing

to the MS. When the measured voltage between the two bellows only differed by $\simeq 50$ mV, a sufficient equal behaviour was achieved.

The crimping was performed at the very beginning of this project, and it has later been observed that this might need to be redone. The pressure adjustment set point is defined as when the RB (containing reference gas) is at 80%. This allows for some variability of sample size as the LB compresses to reach the same voltage point. However, it has been observed through filling the bellows with an equal amount of gas and then performing pressure adjustment, that the LB compresses to $\simeq$65% to achieve the same voltage as the RB. This indicates that the flow is much less constrained for the RB and that this capillary should be crimped some more. The pressure in the bellows while crimping might have been smaller than what is required for measurements, leading to the difference now seen between the two bellows. The pressure gauges in the two bellows also read slightly differently when the bellows are open to the same volume. This pressure difference is however only around 0.5 mBar for the typical working pressure range, and thus it is assumed that this is not the main cause for the imbalance. Though the bellows compress differently, the pressure imbalance correction is still linear (see section 6.2), but for future work it is recommended to recrimp the capillaries for even more robust measurements.

There are some benefits to constraining the flow of both bellows better. One is that there will be less drift in the measured intensity over time as less gas is measured. Since compressing the bellows will give a smaller difference in the measured intensity, it allows for investigating effects due to slight differences in pressure. However, this would give a smaller signal-to-noise ratio of the measurements, and therefore this has not been pursued.

5.2.2 Heating out capillaries

At the beginning of this project, the MS had been idle for some time. During this time, pumps have not been attached to the system and if a small leak is present in the DI system, it was thought that the capillaries might have been contaminated by impurities such as dust or water. To remove the possibility of contamination of measurements, the SST capillaries were heated out.

Dry reference air was allowed to flow through the capillaries, with valves from both bellows open to the vacuum pump located after the crimps. This transports the impurities to the waste line alongside the gas. The crimping blocks were removed during the process. Both the "Inlet Heater" and the "Inlet Valve Heater" of the MS were turned on to heat the surroundings of the capillaries to about 80°C for 45 minutes.

Then two ground banana jacks are hooked up to the changeover valve and two 7.7 V banana jacks are connected to the brass contacts in the center of each capillary. The electric current is then turned on and flows from the center of the capillaries to both of their ends to heat them out. The heating phase lasted 30 minutes while gas continuously flowed through the capillaries.

5.3 The ion source and focus settings

The gas molecules and atoms entering the ion source of the MS are ionized by electron bombardment taking place in the so-called "ionizer housing". The amount of electrons bombarding the gas is determined by the "emission" parameter in the Isodat NT focus settings. A higher emission current results in a higher intensity due to a larger ionization rate, and thus a better signal-to-noise ratio. Achieving high precision measurements also depends on how reliable the ion source is. In the course of this thesis work, several maintenance operations were performed on the ion source.

5.3.1 Repairing and replacing filaments

The lifetime of the tungsten filament providing electrons for ionization is decided by how frequently it is in use and how high the emission current is set. It will, however, degrade over time. Other laboratories exchange the filament every 3-6 months [Oyabu et al., 2020].

The MS interface at all times displays the measured "trap current" and "box current" which are two separate electron currents in the source. When these parameters start to diverge, it typically is a sign that the filament is degrading and should be replaced. During the course of this thesis work, this happened twice. Once it turned out that the filament had become loose in the source and reattaching it solved the issue. The other time, the filament was replaced with a new one.

5.3.2 Focus settings

Small physical or geometrical changes in how the source is placed in the MS can affect the ion beam greatly. Therefore, the beam is focused every time the source has been reinserted in the MS. Isodat NT has an automatic focusing function that attempts at reaching the highest possible measured intensity. When focusing the MS, one can choose to favor either linearity or sensitivity. One is always a tradeoff of the other. In this case linearity refers to the measurement of isotopic or elemental ratios being directly proportional to the gas flow into the MS, which is the kind of focusing the automatic function performs. A loss in linearity also means that one might find that corrections such as the pressure imbalance slope and chemical slope are not linear anymore. However, sensitivity is also favored in some cases. If the peak shapes in dual inlet mode are not square-like, it can be sensible to perform a sensitivity focusing. Here one lowers the so called "Extraction Energy" to improve upon the peak shapes and reliability of the measurement, as shown in the following section.

5.4 Shims and peak shapes

The working point of the MS's high voltage is crucial for reliable measurements. By performing a scan of intensity against high voltage, the optimal working point can be determined by setting the voltage to where the point of best peak alignment. This allows for the beam to diverge somewhat from the magnetic field set point without it affecting the measurement.

However, problems arise when the peak shapes are not square. In this scenario a small fluctuation in the high voltage might result in measurements with large associated uncertainties. This was observed as is shown in figure 5.1. Earlier data from the instrument installation shows that the Delta V Plus had square peak shapes in 2007 (figure 5.2). Since then the instrument has been moved, which may have contributed to varying conditions of the MS.

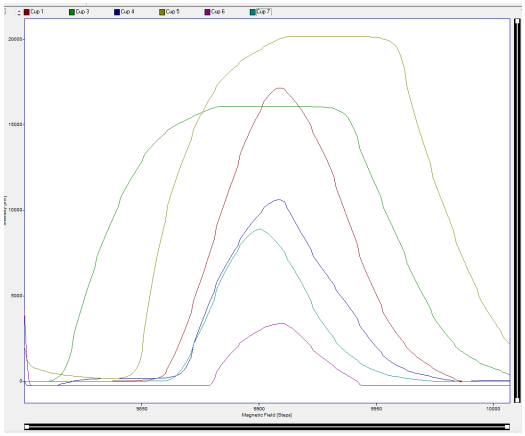

Figure 5.1: Intensity vs magnetic field. $N_2/O_2/Ar$ configuration slow magnet scan in 2020.

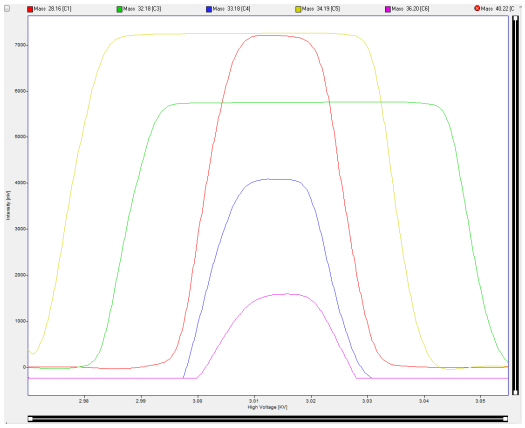

Figure 5.2: Intensity vs magnetic field. $N_2/O_2/Ar$ configuration slow magnet scan in 2007.

Through communication with technical support specialists at Thermo Fisher, installing magnetic shims in the MS was recommended. These shims are metal plates to be installed between the magnets and the analyzer in the flight tube of the magnet section. This is a maintenance operation that improves upon the surface of the analyzer. A picture from the installment of the shims is shown in figure 5.3. Still after installing the shims, the focus settings needed to be tuned manually to achieve square-like peak shapes as is shown in the following.

Figure 5.3: One of two shims placed between the magnet and the analyzer in the flight tube.

5.4.1 Peak shape dependence on extraction parameter

By adjusting the different focus settings, it was found that the parameter "extraction" affected the peak shapes immensly. By lowering the extraction, the peaks became more square-like. Peaks with flat plateaus are important as otherwise small fluctuations or drifts of the magnetic field strength or high voltage can induce large signal variability. To fully gauge this effect, the extraction was varied between 20% and 80% with 20% intervals. An autofocus procedure was done for each of the values for the two used configurations, the peak shape scan performed and then a zero-enrichment measurement was done to gauge what effect the peak shapes have on the standard deviations of the measurements. The peak shapes for the N_2 configurations are shown in Figure 5.4. The same experiment for the $N_2/O_2/Ar$ configuration can be found in A.1. The values resulting from the zero-enrichment tests can be found in Table 5.1. The standard deviation from 80% extraction is between a factor 2 and 4 larger than for the rest of the measurements.

Figure 5.4 shows that even at an extraction of 40 %, the middle cup (green line) does not resemble a square. Procedures for sensitivity focusing have therefore been followed, setting the extraction values at 25% for both the N_2 and the $N_2/O_2/Ar$ configuration. Though the focus settings have been determined with favor of sensitivity, the pressure imbalance tests still show linear trends (see section 6.2), leading to the

conclusion that the linearity has not been reduced largely.

Extraction	20 %	40 %	60 %	80 %
$\delta^{18}O$	-0.04 ± 0.02	-0.02 ± 0.01	-0.03 ± 0.03	-0.08 ± 0.02
$\delta^{15}N$	-0.025 ± 0.008	-0.015 ± 0.004	-0.02 ± 0.02	-0.04 ± 0.01
$\delta O_2/N_2$	-0.076 ± 0.003	-0.041 ± 0.007	-0.07 ± 0.002	-0.202 ± 0.008

Table 5.1: Results of zero-enrichment measurements for different extraction values.

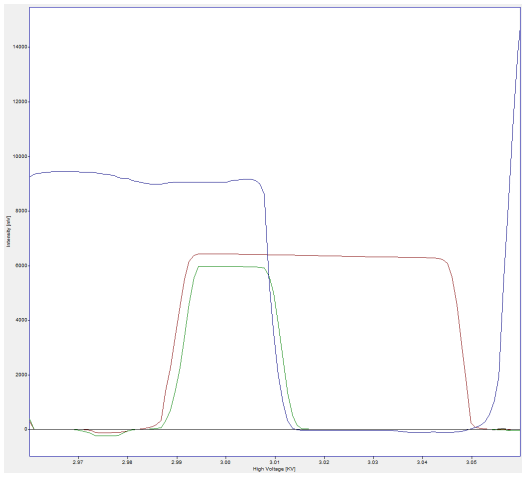

Extraction at 20%.

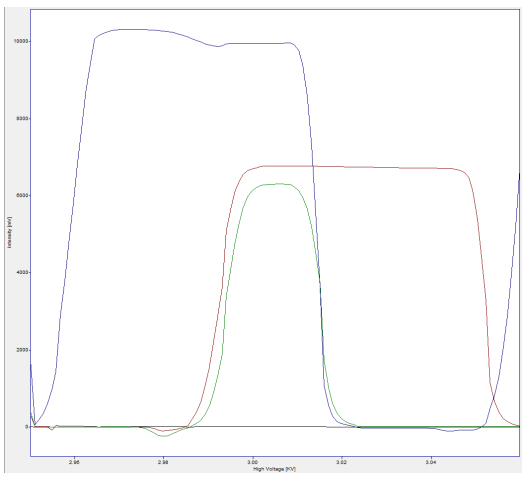

Extraction at 40%.

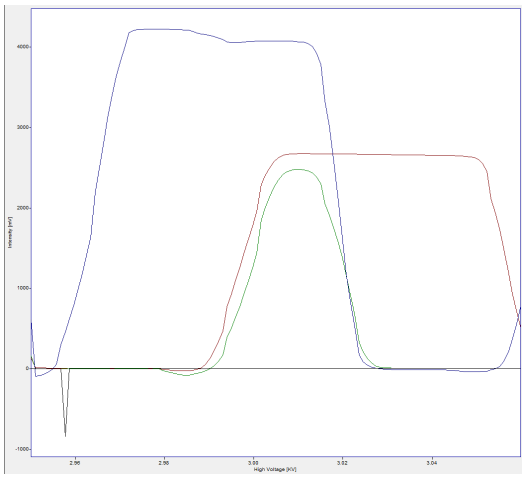

Extraction at 60%.

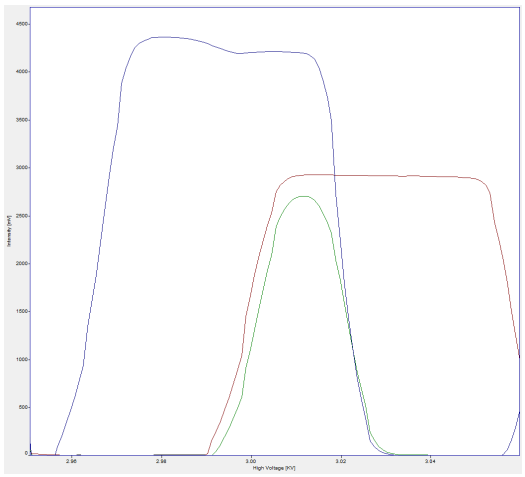

Extraction at 80%.

Figure 5.4: Vertical axes are signal intensities in mV, while the horizontal axes are the high voltage in kV. Red line is m/z 28 (cup 3), green line is m/z 29 (cup 4) and blue line is m/z 30 (cup 5).

6 | Corrections and instrument tests

As mentioned previously, corrections must be applied to the raw MS data to correct for effects due to the instrument and processes inherent to the firn or treatment of the ice core causing fractionation. In this chapter, a closer look on these corrections will be taken. In addition, the reproducibility of the MS will be investigated, and the observed variations serve as the estimated internal precision of the MS.

6.1 Zero-enrichment test

The so-called zero-enrichment test is a useful tool to verify the stability of the MS and indicate possible precision errors on the instrument. The zero-enrichment measurement sheds light on possible fractionations of the sample or standard as they are introduced to the source. These measurements are performed before and after measurements of an ice sample to ensure that the MS is stable over the duration of a sequence.

The measurement has been automated and can be initiated by two rows of a sequence which are present in all sequences used for measurements of samples. Both bellows are filled with the same amount of reference NEEM gas ($\simeq$ 4 cc). Then they are measured against each other by sequentially introducing gas from the sample and standard bellows with the same parameters as described in section 5.1.1. This means that from the measurement both $\delta^{18}O$, $\delta O_2/N_2$ and $\delta^{15}N$ are obtained. The name of the procedure indicates that the sample should not be enriched relative to the reference gas, however, as discussed in the following, some systematic effects are evident.

In figure 6.1, the mean of the $\delta^{18}O$ for different measurement days is shown along with its standard deviation. The same plot is made for $\delta^{15}N$ in figure 6.2. The number of zero-enrichment measurements vary between 2 and 5 for the measurement days.

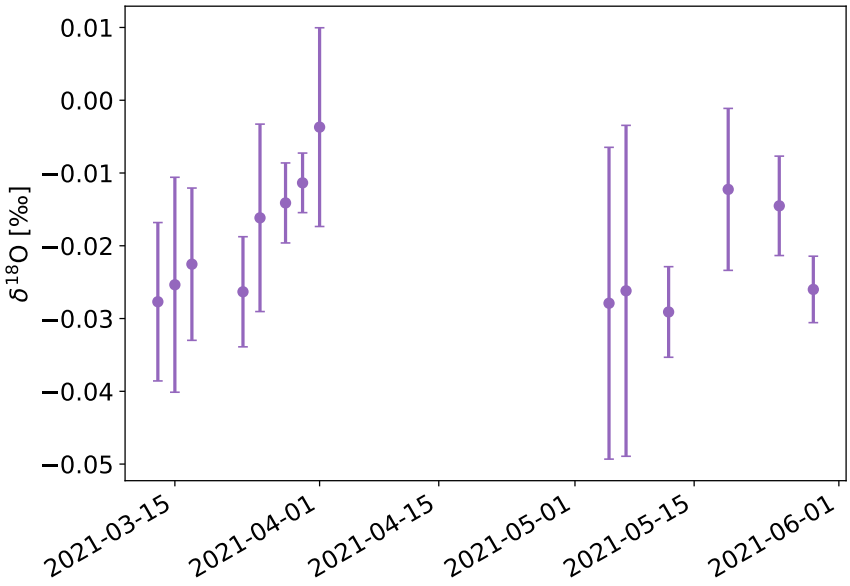

Figure 6.1: Average of δ^{18}O from the zero-enrichment tests made for different measurement days. Error bars indicate the standard deviation of the mean for a certain day.

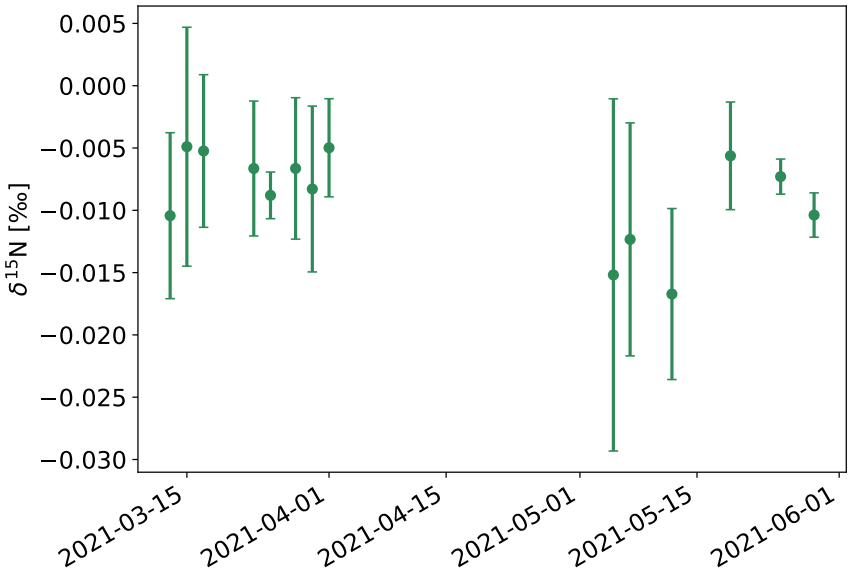

Figure 6.2: Average of δ^{15}N from the zero-enrichment tests made for different measurement days. Error bars indicate the standard deviation of the mean for a certain day.

The pooled standard deviation, σ_{pooled}, represents the long-term internal precision of the instrument and was calculated as follows [Barlow, 1991]

$$\sigma_{\text{pooled}} = \sqrt{\frac{(n_1-1)\sigma_1^2 + (n_2-1)\sigma_2^2 + ... + (n_k-1)\sigma_k^2}{n_1 + n_2 + ... + n_k - k}}, \tag{6.1}$$

where k is the number of measurement days, and n and σ are respectively the number of measurements and standard deviation for a specific day. σ_{pooled} is calculated to be $0.012‰$ for $\delta^{18}O$ and $0.0069‰$ for $\delta^{15}N$.

No drifting trend is observed, supporting that there are no effects changing the internal precision. However, it is seen that all average values are negative. This points to a systematic fractionation effect causing the sample bellow gas to be depleted in the heavier isotopes compared to the reference bellow.

This systematic tendency needs to be taken into account. Therefore, it was decided to apply a zero-enrichment correction to the raw $\delta^{15}N$ and $\delta^{18}O$ values. This is done by averaging the obtained zero-enrichment values for the measurement day and subtract them from the raw sample measurement, $\delta^{18}O_{\text{raw}}$, as

$$\delta^{18}O_{\text{z.e. corrected}} = \delta^{18}O_{\text{raw}} - \delta^{18}O_{\text{z.e. mean}}, \tag{6.2}$$

where $\delta^{18}O_{\text{z.e. mean}}$ is the average of all zero-enrichment values of $\delta^{18}O$ from that day. The same correction is applied to the $\delta^{15}N$, resulting in a $\delta^{15}N_{\text{z.e. corrected}}$ that is later used for gravitational correction of $\delta^{18}O$. These corrections typically increases the value of $\delta^{18}O$ by $0.02‰$ and $\delta^{15}N$ by $0.01‰$ as can be seen from figures 6.1 and 6.2.

6.2 Pressure imbalance correction

It is known that the measured δ-values are sensitive to flow changes into the ion source. Though the bellows are balanced to reach the same intensity in the source of the MS, it is not in practice feasible to exactly balance the ion currents of the sample and reference. Capillaries leading the gas from the bellows to the MS are crimped by hand, and thus are likely to allow slightly different gas flows as discussed in section 5.2. The bellows also possibly contain different volumes. As alluded to in previous chapters, these effects can be corrected for by a linear pressure imbalance (PI) estimation. This is assuming that the inequalities are not diverging beyond reason.

To monitor how the δ values vary with different pressure in the source, both bellows are filled with reference gas as for the zero-enrichment test. Then the pressures in the sample and standard bellows are unbalanced. The standard bellow is pressure adjusted to reach the relevant intensity on cup 4 which means its position is typically at 80%. The sample bellow is varied in steps from 100% to 60% and back to 100%

again. The resulting measured δ^{18}O is then evaluated against the intensity difference of $m/z = 32$ of the reference and sample bellows.

A linear fit is made to the collected data, and its slope is used for correcting δ^{18}O of gases in ice core samples. In doing this, an underlying assuption is that the pressure imbalance related δ deviation varies linearly with pressure imbalance. This has been supported experimentally by e.g. [Bender et al., 1994b].

An example of a pressure imbalance measurement is shown for δ^{18}O in figure 6.3. Here the slope of the linear dependency, α, is $2.7 \cdot 10^{-4}$ ‰·mV^{-1} which is a typical value for our system. Notice that the data extends to the case where the intensities of sample and reference bellow are imbalanced by 5000 mV. This is a very unrealistic case, but verifies that the effect is still linear for large pressure imbalance ranges

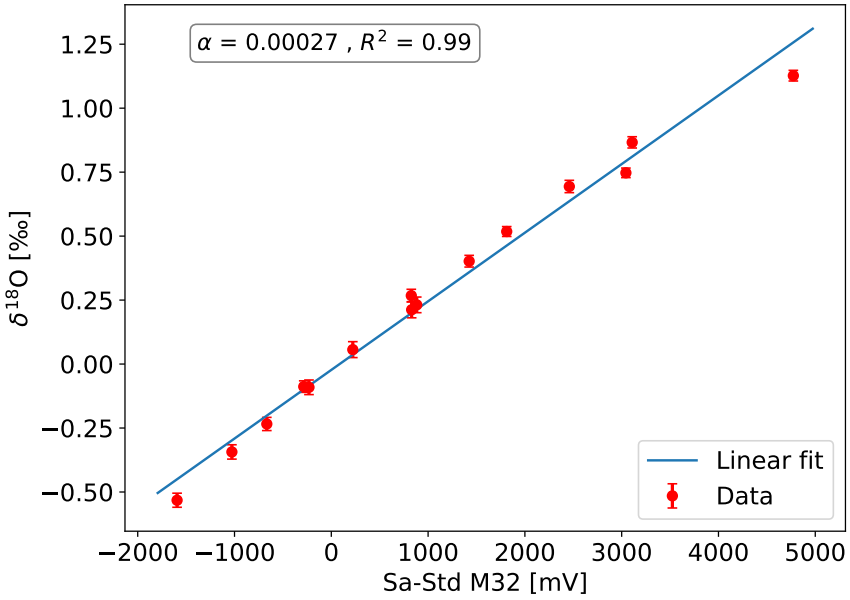

Figure 6.3: Pressure imbalance data with a linear regression fitted to it from 01.06.2021.

The PI effect may vary with time, and other studies have typically performed a PI test on a weekly basis [Severinghaus et al., 2003, Grzymala-Lubanski, 2015]. Then the effect is assumed not to vary on faster than weekly time scales. In this project, however, it was decided to perform a PI test every day of measurements to obtain a daily correction to the measurements. Results from PI tests over the month where RECAP samples were measured can be seen in table 6.1. The slope, α, is similar over the measurement days, confirming the assumption that it does not tend to vary much over a week.

α (‰· mV^{-1})	R^2 of linear regression	Date
$2.81{\cdot}10^{-4}$	0.987	06.05.21
$2.71{\cdot}10^{-4}$	0.976	25.05.21
$2.59{\cdot}10^{-4}$	0.976	28.05.21
$2.68{\cdot}10^{-4}$	0.985	01.06.21

Table 6.1: Results from PI tests over the month where the system was used for measurement of RECAP samples. The PI slope is decided by a least-square fit.

When the PI slope is determined for a certain measurement day, $\delta^{18}O_{\text{z.e. corrected}}$ can be corrected as

$$\delta^{18}O_{\text{PI corrected}} = \delta^{18}O_{\text{z.e. corrected}} - \alpha \cdot \Delta V, \tag{6.3}$$

where ΔV is the difference in intensity between the sample and standard bellow.

6.3 Chemical slope measurement

Due to non-linearity in the ion source, isotopic ratios are sensitive to changes of the gas composition of the sample. To account for this measurement artifact in the MS, the so-called chemical slope (CS) must be assessed [Severinghaus et al., 2003].

To quantify the chemical slope for $\delta^{18}O$, one measures the reference gas against a sample that resembles the reference gas but is increasingly enriched in N_2. In previous work on the setup, this mixing has been done externally in a line leading to the MS. The procedure demanded that the gases were mixed manually, which turned out to be very time-consuming. It was therefore decided to automate the procedure to become more reliable and able to more quickly measure over a larger range of $\delta O_2/N_2$.

A new procedure for gauging the CS effect was developed with inspiration from [Huber and Leuenberger, 2004]. The reference bellow is filled with NEEM reference gas at the normal working pressure ($\simeq$40 mBar). The sample bellow is filled with pure N_2 at low pressure ($\simeq$ 2 mBar). For the reference measurements, the reference bellow is opened to the MS as per usual. However, when measuring the sample, both valves leading to the changeover from the bellows are open at the same time. This allows for dynamic mixing of the pure N_2 and NEEM reference air while being introduced to the MS. The reference bellow is kept at a constant pressure, while the sample bellow is compressed to enrich the sample with an increasing amount of N_2, resulting in a larger negative $\delta O_2/N_2$.

As aforementioned in section 5.1, the original programming in Isodat increased the bellow position to 100% before decreasing to whatever set point was decided in the sequence. It became evident during testing the CS procedures that this kind of violent mixing causes kinetic fractionation.

In Figure 6.4, two chemical slope tests from two different days are shown. The tests also differ in that two different ranges were measured for the chemical slope i.e. different amounts of N_2 in the sample bellow. The color of the data points becomes darker for later measurements in the sequence. The reason why $\delta O_2/N_2$ does not vary much at the end of the sequence is that gas loss during measurements cancels out the effect of compressing the bellow when there is very little gas left in the bellow. This effect should, however, not affect the linearity of the slope of the test. The CS measurement begins with the sample bellow at 100% and decreases to 10%. No unambiguous value of $\delta^{18}O$ for a certain of $\delta O_2/N_2$ is seen at the end of the sequence. It was found that this was because the bellow increased to 100% before decreasing to the set position which causes fractionation. The two linear fits where β is the slope have smaller values of R^2 than what was found for the PI tests, indicating that the dependency is less linear. The figure is merely included for illustrating that this kinetic fractionation effect in the bellows when their positions differ too much without giving the gas time to equilibrate again.

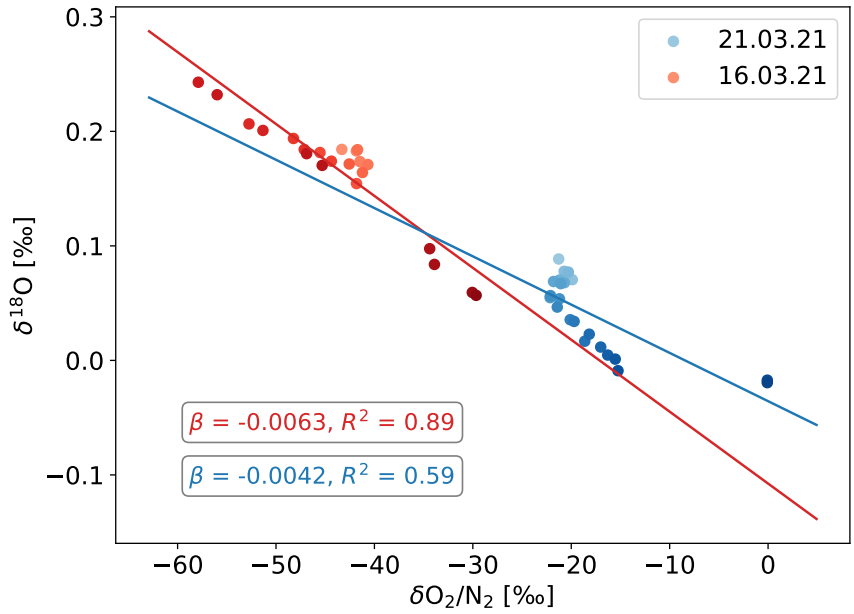

Figure 6.4: Combined chemical slope test for 16.03.21 and 21.03.21. The data is not corrected for pressure imbalance, and the plot is merely included for illustrating the effect of kinetic fractionation in the bellows when compressed.

After changing the default ISL script for manually adjusting the bellows from Thermo Fischer (see section 5.1), this kinetic fractionation effect disappeared. In Figure 6.5, the data from a PI corrected CS test is shown along a linear function fitted to the data. The R^2 value of 0.98 indicates that a linear model is suitable for this data.

The CS is specific to the MS and may vary over time, much like the PI effect. Therefore CS tests were conducted before and after measuring the RECAP samples. This amounts to two tests a week.

After the CS slope, β, is found, $\delta^{18}O_{\text{CS corrected}}$ can be found by

$$\delta^{18}O_{\text{CS corrected}} = \delta^{18}O_{\text{PI corrected}} - \beta \cdot \delta O_2/N_{\text{2grav. corrected}}, \tag{6.4}$$

where $\delta O_2/N_{\text{2grav. corrected}}$ is corrected as described in the next section. Notice that the CS parameter β is found for data that is also corrected for pressure imbalance. There is really no reason that the PI correction must be done before the CS correction, but if one chooses to reverse the order, the PI data must be corrected for the CS effect.

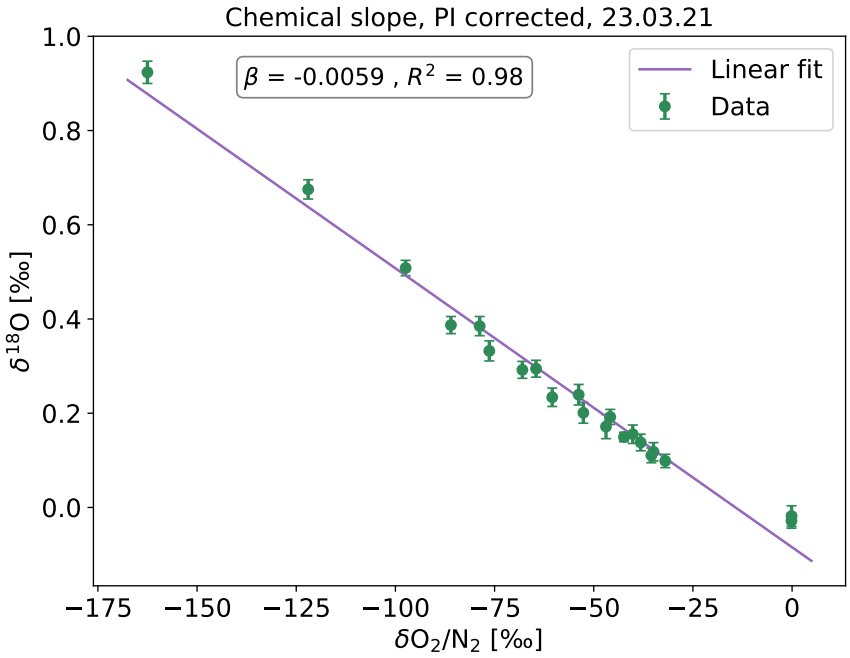

Figure 6.5: Chemical slope test from 23.03.21 where the data has been corrected for pressure imbalance effects. The errorbars indicate the standard deviation on the $\delta^{18}O$ measurement.

6.4 Chemical slope for $\delta^{15}N$

The measured $\delta^{15}N$ is only corrected by the zero-enrichment correction. To gauge whether $\delta^{15}N$ should be corrected for a chemical slope as well, a similar measurement as described in the previous section was performed. Instead of filling the sample bellow with N_2 it is filled with O_2 at similar pressure as for a normal CS test. This gives a chemical slope with an oxygen-enriched sample. Then the same measurement procedure as for the $\delta^{18}O$ chemical slope of $\delta O_2/N_2$ is followed. The result is shown in Figure 6.6, where no linear trend is detectable. No pressure imbalance correction has been applied to this data, but doing so would not change the linearity. It was therefore concluded that no CS correction needs to be applied for $\delta^{15}N$.

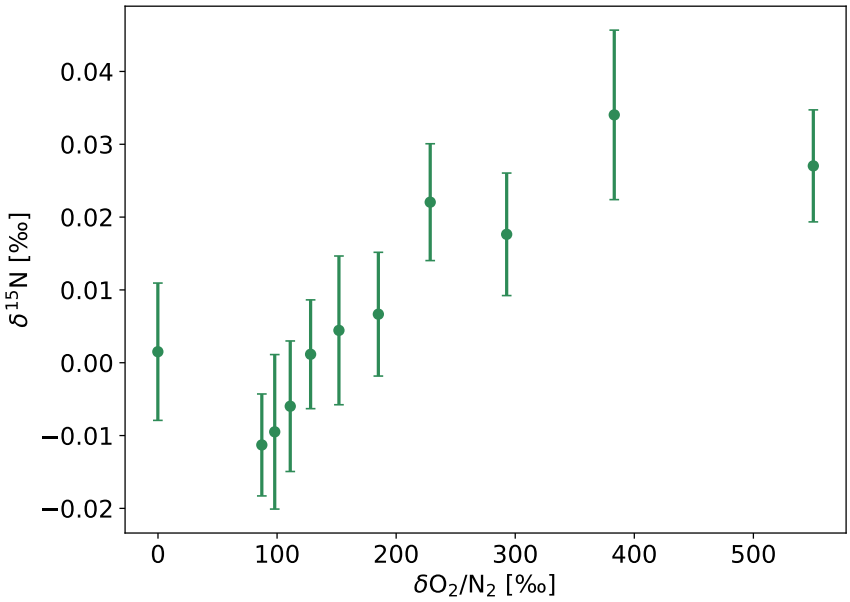

Figure 6.6: δ^{15}N is plotted as a fuction of $\delta O_2/N_2$.

6.5 Mass dependent fractionation

After correcting for instrument effects, fractionation happening in the firn can be taken into account. The gravitational correction as discussed in section 2.2 is by far the largest correction applied to the data. Following Eq. 2.6, $\delta^{18}O_{\text{grav. corrected}}$ can be found as

$$\delta^{18}O_{\text{grav. corrected}} = \delta^{18}O_{\text{PI corrected}} - 2 \cdot \delta^{15}N_{\text{z.e. corrected}}. \tag{6.5}$$

Following the same procedure, the gravitational correction for $\delta O_2/N_2$ is

$$\delta O_2/N_{2\text{grav. corrected}} = \delta O_2/N_2 - 4 \cdot \delta^{15}N_{\text{z.e. corrected}}. \tag{6.6}$$

Though this correction is based on an assumption that δ^{15}N only stems from gravitational effects, it may also remove fractionation processes that generally scale with mass difference Δm.

The gravitational correction is the final correction made to the data in this project. Other studies have developed methods for correction of effects such as bubble-close off fractionation [Severinghaus and Battle, 2006] and gas loss [Severinghaus et al., 2009]. However, these are found to be negligible for this project.

6.6 Effect of CO_2 on $\delta^{18}O$ measurements

Previous measurements with the system were conducted with CO_2 free air on the sample site while CO_2 was not removed from the reference gas. In [Grzymala-Lubanski, 2015] it is argued that the effect of CO_2 on $\delta^{18}O$ is so small that there is no need neither for removing it from the standard gas nor correcting for it. However, as this might violate the identical treatment principle, it was decided to investigate the effect of CO_2 on $\delta^{18}O$ and possibly remove CO_2 from the reference gas as well.

To gauge whether CO_2 has an effect on the measured $\delta^{18}O$, CO_2 was measured by peak jumping on cup 4 with its mass to charge ratio $m/z = 44$ following [Melissa Anne Headly, 2008]. The relationship between $\delta^{18}O$ and rCO_2 is shown in figure 6.7, where rCO_2 is the ratio of CO_2 of the sample to the standard. A linear fit is made to the data with an $R^2 = 0.96$, indicating that a linear model is reasonable for the relationship and more importantly showing a high correlation between $\delta^{18}O$ variability and CO2. At $rCO_2 = 1$, one would expect $\delta^{18}O$ to go to zero, which is not the case as the function obtained from the fit indicates a $\delta^{18}O = 0.075‰$ here. It should also be noted that in this test, the sample is enriched with CO_2, where in previous measurements the sample has been depleted in CO_2. Thus, the measurement is showing an unrealistic region for rCO_2, as the reference in previous measurements has been enriched in CO_2 and not depleted compared to the sample. However, it was concluded that difference in CO_2 levels in standard and sample does have a non-negligible impact on $\delta^{18}O$. To account for this and honor the principle of identical treatment, a chemical CO_2 trap was made and installed on the line leading from the gas container of dry NEEM air to the MS. The design of the trap is described in detail in Section 4.11.

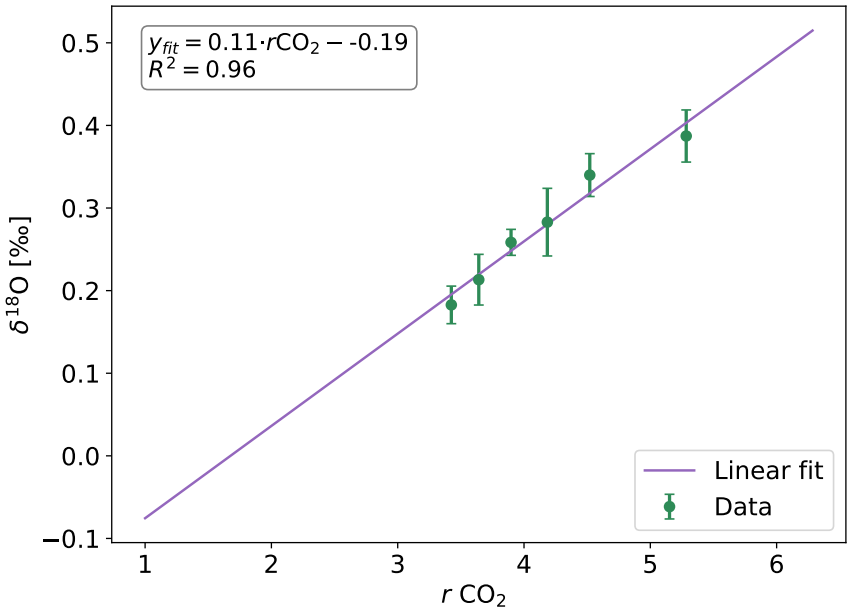

Figure 6.7: $\delta^{18}O$ is plotted as a fuction of δCO_2. A linear fit to the data is also shown.

7 | Test ice measurements and external precision

A quantification on how the different components of the experimental setup are performing is needed. In the previous chapter, the zero-enrichment measurements served as an assessment of the internal precision or measurement uncertainty on dry gas in the MS.

In this chapter, the "external" parts of the experimental setup are included and thus the external precision evaluated. These components are sections of the setup that are not included in the MS for the δ^{18}O configuration of the line (figure 4.1). The rod variability will be assessed by measurements of dry air collected in the dip tubes. Then a complete estimate on the external precision will be made based on extraction, collection and measurement of air in recent Holocene ice samples from the NEEM ice core.

7.1 Dry air measurements

Prior to measuring gases extracted from bubbles in ice, the setup was tested with measurements of dry NEEM standard gas[1]. A sample of 4 cc of reference gas is flowed through the MFC (figure 4.1). The gas passes through T3 where CO_2 is removed and is trapped in a dip tube. Then the air is expanded to and measured by the MS. All evaluated values ($\delta^{18}O$, $\delta O_2/N_2$, δ^{15}N) should be close to zero as the gas is the same in both bellows. This was done to quantify possible fractionation originating from the line or dip tubes.

The measurement order of the samples in the dip tubes was mixed up between different test days and between every three samples a zero-enrichment measurement was performed to verify the stability of the MS. The results for δ^{18}O are presented in figure 7.1. No corrections have been applied to the data.

In table 7.1, the standard deviations resulting from the measurements presented in figure 7.1 can be found. The dip tubes 4, 5 and 10 have a larger variability than the accepted 0.05‰ for δ^{18}O as mentioned in section 4.1. Rods 2, 3, 6, 7, 8 and 9 have $\sigma_{\delta^{18}O} < 0.05‰$. Rods 6, 8 and 9 further have $\sigma_{\delta^{18}O} < 0.03‰$. These three rods were

[1]This gas originates from the same bottle that is used as reference gas in the dual inlet MS.

therefore used for ice measurements and δ^{18}O for the three rods are plotted in figure 7.2. Rods 6, 8 and 9 also have the smallest variability for δ^{15}N with $\sigma_{\delta^{15}\mathrm{N}} < 0.01‰$.

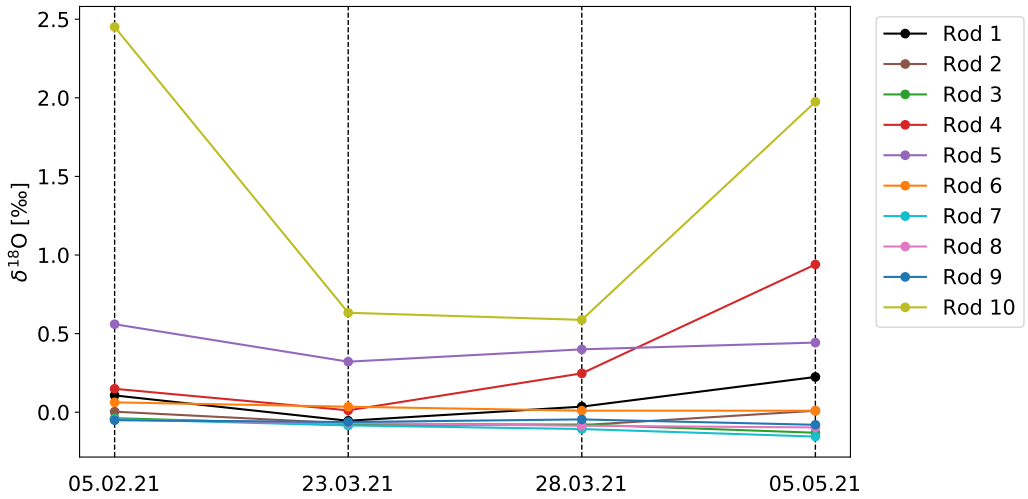

Figure 7.1: δ^{18}O for the ten rods measured at different times throughout the project.

Rod nr	$\sigma_{\delta^{18}\mathrm{O}}$ [‰]	$\sigma_{\delta^{15}\mathrm{N}}$ [‰]
1	0.102	0.0678
2	0.0419	0.0205
3	0.0322	0.0134
4	0.358	0.218
5	0.0862	0.0491
6	**0.0287**	**0.00328**
7	0.0381	0.0172
8	**0.0178**	**0.00668**
9	**0.0133**	**0.00743**
10	0.819	0.478

Table 7.1: Standard deviations for each rod resulting from the measurements made throughout the project.

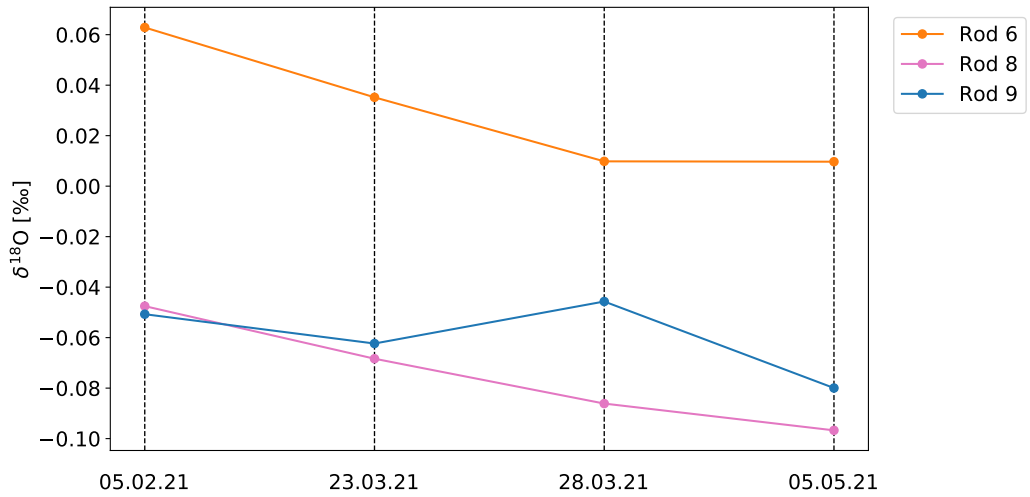

Figure 7.2: δ^{18}O for rods 6,8 and 9 measured at different times throughout the project.

The pooled standard deviation of measurements of dry air in the dip tubes is found by Eq. 4.1 to be 0.0256‰ for δ^{18}O and 0.00743‰ for δ^{15}N. This is the variability due to the rods.

7.2 Bubble free ice

To fully respect the identical treatment principle, a reference that has been subjected to the exact same processes as the sample would be ideal. A perfect standard would be air of known composition enclosed in bubbles in ice. The gas would be extracted in the exact same way as the sample and measured as the standard in the reference bellow. The second best reference gas is gas that is flowing to the system at the same time as bubble free ice (BFI) is melted.

Several attempts were made to create such a standard. At PICE, the BFI is made by degassing milli-Q (ultrapure) water under vacuum by evacuating the water container. At the same time the water is heated and stirred to release gases. Then the water is freezed from the bottom up. This is done by placing the water vessel inside a freezer with a heat jacket on. The heat jacket is slowly lifted up, allowing the water at the bottom to freeze. This method creates ice that by visible inspection contains no bubbles.

The reference gas on top of BFI was measured by two methods. Both experiments use samples of BFI at the same weight as a normal sample ($\simeq$ 40 g). Notice that since these are not porous, they tend to require a longer melt time, as the surface area is smaller and there is a lower chance for the ice breaking into smaller pieces during the melt. In both methods, the extraction time was 15 minutes after the ice is completely melted, as is the usual procedure for measurements.

In the first experiment, NEEM reference gas is flowed through the MFC into an

open vessel containing a BFI sample until the vessel contains 4 cc of air. Meanwhile the vessel is kept in the cold ethanol bath used for preserving the ice samples. The valve of the vessel is closed, the line leading to the MFC evacuated, and the normal procedures for melting ice and extracting air is followed. This leads to a sudden spike in pressure as all the gas is let out of the vessel simultaneously instead of in the gradual way as it would be when enclosed in bubbles. Measuring the resulting sample gave widely varying results that do not resemble the reference (table 7.2).

A second version of the BFI experiment was therefore conducted. Through the MFC, 4 cc of NEEM reference gas was flowed at a rate of 0.8 cc/min, leading to a flow time of 5 minutes to resemble the melt time. This was done while the BFI ice was melted, therefore creating a synthetic replicate of a typical ice melt. Though this method resembles the real melting procedure, measurements resulting from this experiment were also wildly variable (table 7.2).

Rod nr	δ^{18}O [‰]	δ^{15}N [‰]	Experiment
1	-0.136	-0.0379	1
3	0.0214	0.0428	1
3	0.594	0.415	2
9	-0.0983	0.00370	2

Table 7.2: Measurements of δ^{18}O and δ^{15}N from reference over BFI experiments.

It was concluded after these two experiments, that the BFI is probably not gas free - though it is bubble free. Gases that are occluded in the ice may fractionate the sample heavily.

7.3 NEEM and external precision

By the zero enrichment tests, the internal precision of the MS was found to be 0.012‰ for δ^{18}O and 0.0069‰ for δ^{15}N. By testing the variability of the dip tubes, it was found that the dip tubes numbered 6, 8 an 9 had the smallest variability with standard deviations $\leq$ 0.03‰ for δ^{18}O and $\leq$ 0.01‰ for δ^{15}N. These have been further evaluated by measurements of NEEM ice. In table 7.3, the most recent measurement data for NEEM ice are shown.

The pooled standard deviation for the case of duplicate measurements is

$$\sigma_{\text{pooled}} = \sqrt{\frac{\sigma_6^2 + \sigma_8^2 + \sigma_9^2}{3}}, \tag{7.1}$$

where σ_i is the standard deviation of the duplicate measurements from rod nr i as shown in table 7.3. This results in a pooled standard deviation $\sigma_{\text{pooled}} = 0.031$‰ for δ^{18}O and $\sigma_{\text{pooled}} = 0.023$‰ for δ^{15}N. This is thus the total external precision of the

Rod nr	δ^{18}O [‰]	δ^{15}N [‰]	$\delta^{18}O_{\text{grav corr}}$ [‰]
6	0.613	0.295	0.0175
	0.693	0.372	-0.0513
8	0.565	0.253	0.0587
	0.558	0.264	0.0305
9	0.567	0.264	0.0389
	0.534	0.285	-0.0367

Table 7.3: Measurements of δ^{18}O from recent Holocene NEEM ice. The gravitational corrected data is also Z.E. corrected.

instrument for ice measurements and will be considered as the uncertainty on the RECAP measurements.

Notice that the δ^{15}N values vary from the expected 0.27‰. This indicates that there is some mass dependent fractionation process present in the setup. However, by applying the mass dependent correction for δ^{18}O, this cancels out.

The NEEM measurements presented in table 7.3 were conducted at the final configuration of the experimental setup. This is after the additional water trap was included and a final robust extraction procedure was established. Before this, 13 samples of NEEM were measured which showed a large variability of δ^{18}O and unlikely δ^{15}N values. δ^{15}N should be 0.27‰, but varied between 0.02‰ and 0.79‰. This data can be found in A.1.

7.4 Uncertainty attribution

Evaluation of how the different components of the setup contribute to the total external precision is important to figure out which parts must be optimized. The internal precision, σ_{internal} of the MS has been determined by zero-enrichment measurements. Dry gas was collected in the dip tubes to assess the rod variability, σ_{rods}. Finally, NEEM measurements were conducted to gauge the total external precision, σ_{external}. Any contribution to the total external precision that does not stem from the MS or the dip tubes must be due to the line (extraction and water traps).

	Total external precision	Rod variability	Internal precision	Extraction variability
δ^{18}O	0.031‰	0.026‰	0.012‰	0.013‰
δ^{15}N	0.023‰	0.0074‰	0.0069‰	0.021‰

Table 7.4: Overview of the estimated uncertainties due to the different components of the setup.

By assuming the uncertainties are Gaussian and uncorrelated, the total external precision can be described as

$$\sigma_{\text{external}} = \sqrt{\sigma^2_{\text{internal}} + \sigma^2_{\text{rods}} + \sigma^2_{\text{extraction}}}, \tag{7.2}$$

where $\sigma^2_{\text{extraction}}$ is the variability due to the extraction and water traps. By solving Eq. 7.2 for $\sigma^2_{\text{extraction}}$, $\sigma^2_{\text{extraction}}$ is found to be 0.013‰ for $\delta^{18}O$ and 0.021‰ for $\delta^{15}N$. This indicates that the extraction and water traps contribute more to the uncertainty for δ^{15}N than for $\delta^{18}O$.

8 | RECAP measurements

8.1 Results

The gas age for the deepest part of the RECAP ice core has not yet been established. This chapter combines unpublished $\delta^{18}O$ measurements conducted at Penn State University (PSU, figure 8.1) and $\delta^{18}O$ conducted at NBI-PICE to construct the gas age for the Marine Isotope Stage (MIS) 5 to 5e 70-120 ka.

An enrichment in $\delta^{18}O$ for the PSU data can be seen around a depth of 554 m. To verify that this is the case, six samples in this region have been measured by the system at NBI-PICE during this project.

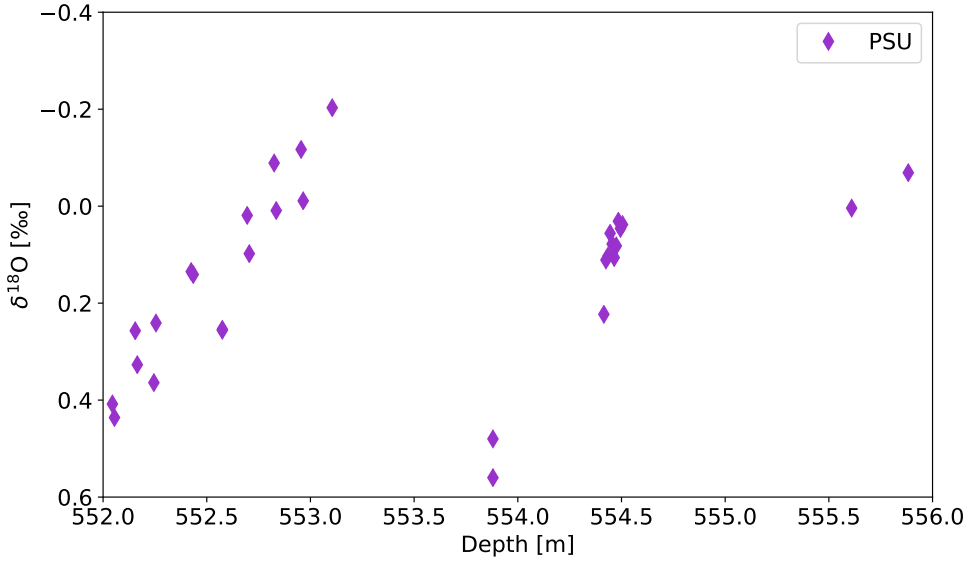

Figure 8.1: Atmospheric $\delta^{18}O$ plotted against depth for the RECAP ice core. Measurements by PSU.

The results of these measurements can be seen in table 8.1. In the table only the final $\delta^{18}O$ after all corrections are presented along with the raw measurements of $\delta^{15}N$ and $\delta O_2/N_2$. In addition, the rod in which the gas was captured is stated and the relationship between the weight of the sample, m, and the resulting pressure in the sample bellow, P, is given.

Depth [m]	$\delta^{18}O_{corrected}$ [‰]	$\delta^{15}N$ [‰]	$\delta O_2/N_2$ [‰]	Rod	m/P [g · mBar^{-1}]
553.060	0.44±0.03	0.296	3.19	6	0.85
553.335	0.14±0.03	0.189	-2.35	8	0.91
553.590	0.36±0.03	0.334	1.10	9	0.86
553.740	0.01±0.03	0.205	-4.59	8	0.95
554.088	0.35±0.03	0.171	4.96	9	0.92
554.150	0.24±0.03	0.239	4.04	6	0.93

Table 8.1: Measurements obtained from the RECAP samples.

The results presented in table 8.1 are plotted alongside the $\delta^{18}O$ data from PSU in figure 8.2. The zero-enrichment corrected $\delta^{15}N$ is plotted alongside the PSU $\delta^{15}N$ in figure 8.3.

An enrichment in $\delta^{18}O$ can be verified for this interval. The $\delta^{15}N$ measured at NBI-PICE also agree well with the PSU measurements. Variations in $\delta^{15}N$ are typically caused by changes in the firn properties due to changes in accumulation and temperature.

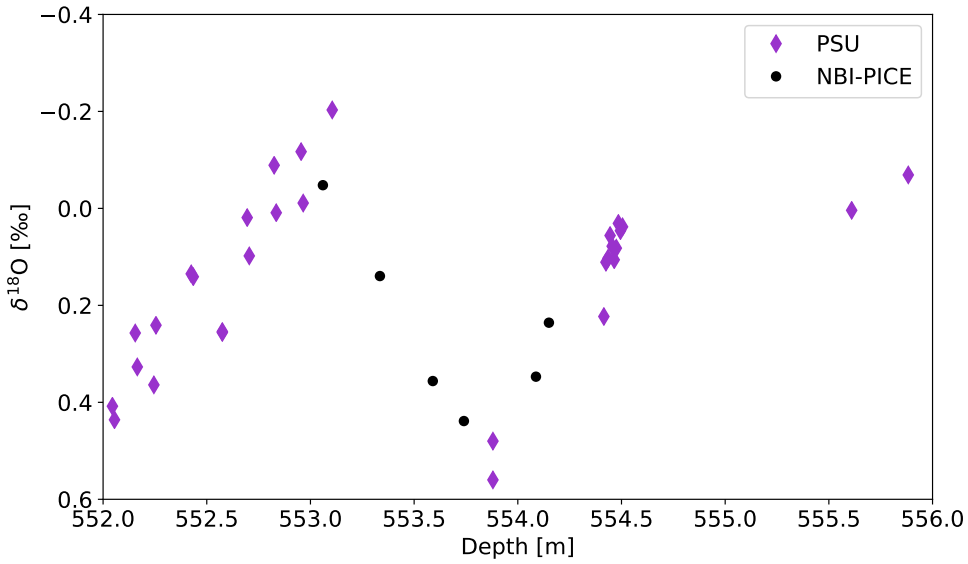

Figure 8.2: Atmospheric $\delta^{18}O$ plotted against depth for the RECAP core. Measurements from this thesis work (NBI-PICE) are black, while from PSU are purple.

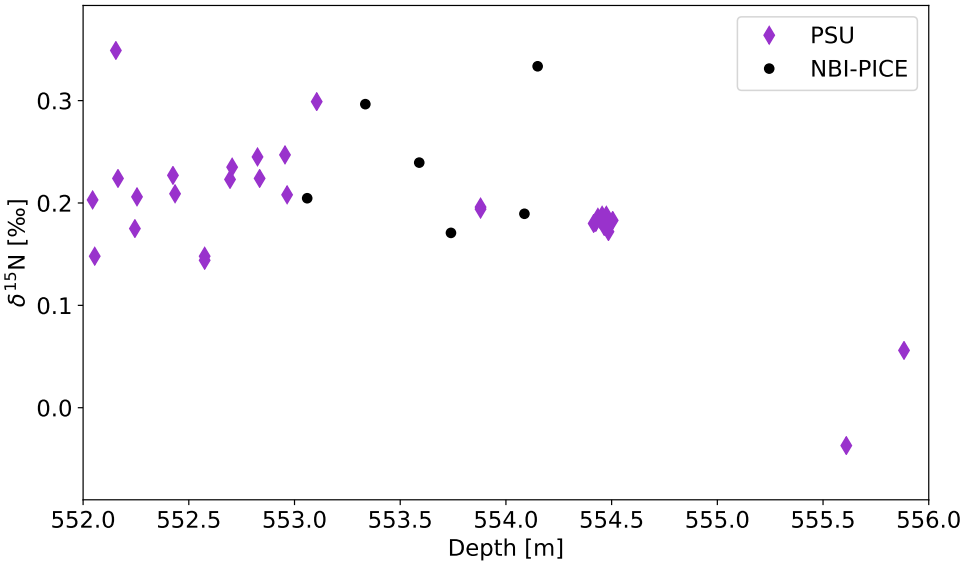

Figure 8.3: δ^{15}N is plotted against depth for the RECAP core. Measurements from this thesis work (NBI-PICE) are black, while from PSU are purple.

The data presented in table 8.1 and plotted in figure 8.2 have been corrected for all effects as discussed. To see how much the different corrections alter the raw measured value, δ^{18}O is plotted at all stages in figure 8.4. It is clear that the gravitational correction has the largest impact and that the other corrections tend to shift the data towards higher values of δ^{18}O.

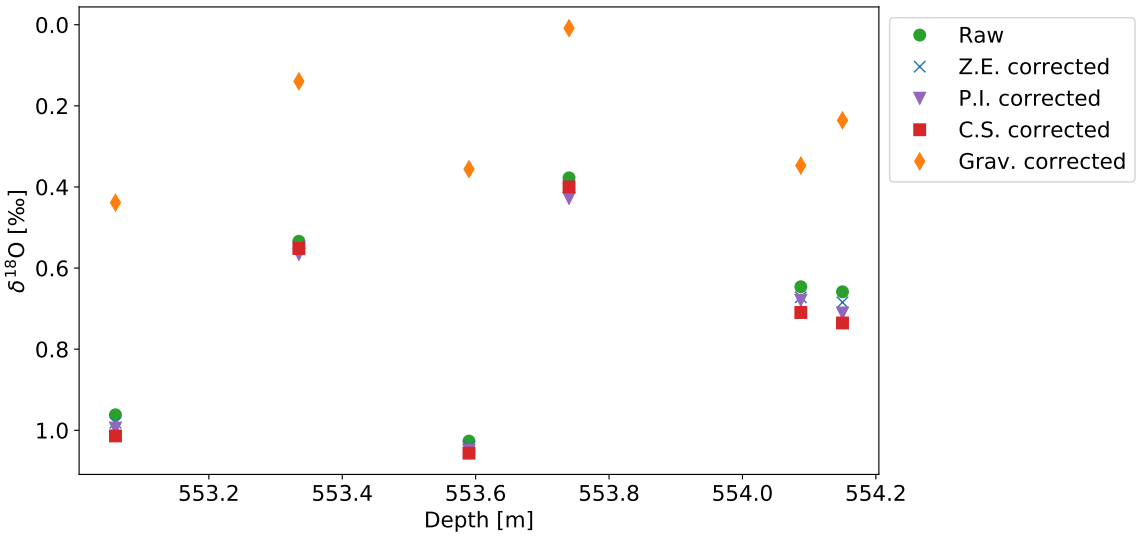

Figure 8.4: The measured δ^{18}O and its corrections plotted against depth for the RECAP core.

8.2 Determination of gas age

Oxygen is a globally mixing gas that allows for synchronizing ice core records across hemispheres. In the following, the already established age scale for the Antarctic EDML core [Veres et al., 2013] will be used to estimate the gas age of the PSU and NBI-PICE samples of the RECAP ice core. The EDML ice core is chosen as reference record because it contains the highest resolution of δ^{18}O for the time period of interest (MIS5-5e) [Capron et al., 2010].

The measured δ^{18}O of the EDML core is plotted against gas age in figure 8.5 as indicated by red markers. This data will be used to map both the RECAP and the PSU measurements to the EDML record's already established time scale following a method used in other studies [Dyonisius et al., 2020]. The data obtained from the EDML core is used to create synthetic δ^{18}O records of a higher resolution by a bootstrapping method [Efron, 2003]. This is done by perturbing every obtained data point as

$$\delta^{18}\mathrm{O}_{\mathrm{EDML}} + G(\sigma), \tag{8.1}$$

where $G(\sigma_{\mathrm{EDML}})$ is a random number picked from a Gaussian function of a certain $delta^{18}$ where its standard deviation is the measurement error from the EDML data, $\sigma_{\mathrm{EDML}} = 0.06‰$ [Capron et al., 2010].

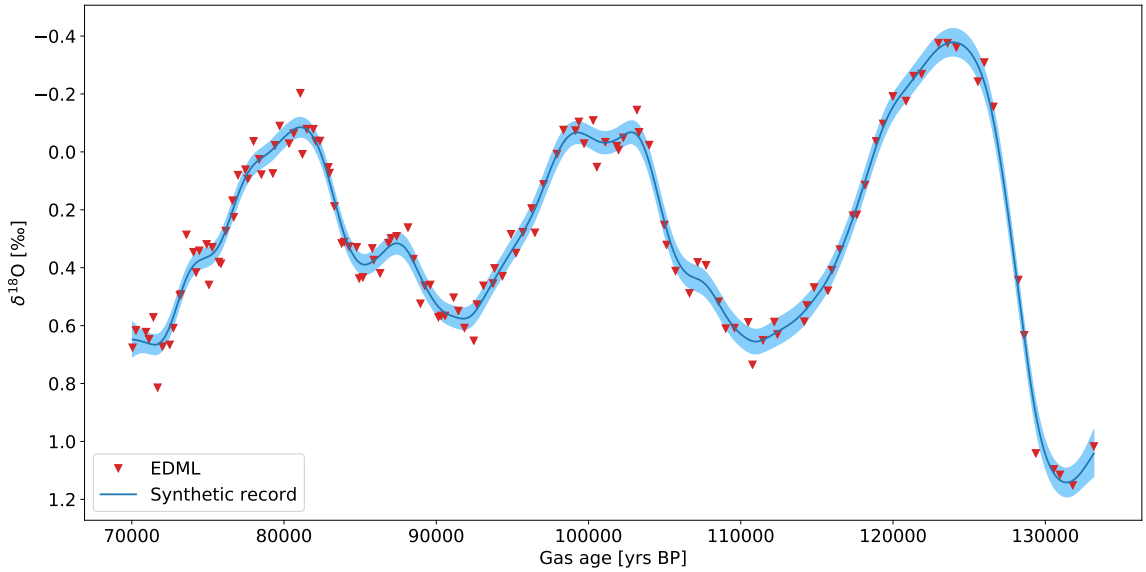

Figure 8.5: In blue is the mean of 10,000 synthetic generated records where the standard deviation is shaded. The red markers indicate the measured EDML δ^{18}O against gas age.

For every perturbed data set, a synthetic high-resolution record is created by interpolation of the data using the `csaps` (cubic smoothing spline) package in Python. After

creating 10 000 synthetic data sets, the mean and standard deviation of the synthetic EDML δ^{18}O are calculated. The resulting data is plotted in figure 8.5 where the variation from the mean by two standard deviations is shaded in blue. Thus, a high resolution record based on the EDML data is obtained that can be used to determine the gas ages for the RECAP samples.

To find what ages in the synthetic record fit best with the RECAP results a "fit vector", $F(t)$, is calculated for every measurement, $\delta^{18}\mathrm{O}_i$, as

$$F(t) = \sqrt{\frac{\left[\delta^{18}\mathrm{O}_i - \delta^{18}\mathrm{O}(t)_{\mathrm{reference}}\right]^2}{\sigma_i^2 + \sigma(t)^2_{\mathrm{reference}}}}, \tag{8.2}$$

where $\delta^{18}\mathrm{O}_{\mathrm{reference}}$ and $\sigma_{\mathrm{reference}}$ originate from the synthetic record and t denotes the age. From $F(t)$, the probability, $P(t)$, of the sample being of a certain age can be derived by

$$P(t) = \frac{\frac{1}{F(t)^2}}{\sum \frac{1}{F(t)^2}}. \tag{8.3}$$

Both $F(t)$ and $P(t)$ are generated uniquely for every sample within determined age bounds. This is necessary to avoid several maxima of $P(t)$ for a sample. The age bounds are based on the assumption that the enrichment of δ^{18}O seen at a depth of 554 m for the RECAP measurements corresponds to the enrichment of the EDML ice core at around 10 kyrs BP. Thus the four measurements from NBI-PICE at shallower depths are assumed to belong to the left flank (younger than the maximum) and the two samples from greater depths to belong to the right flank (older than the maximum).

Through random sampling from the probability distribution $P(t)$, 10 000 samples of possible ages are generated. The resulting histograms are plotted in figure 8.6. These all show single peaks that indicate the age estimation of the sample.

The gas age of the sample is determined to be the year of highest count. The randomly sampled data sets are sorted and the final age bound is found by creating a cutoff at 97.5% and 2.5% of the counts. Thus 95% of the data are allowed to be contained in the age estimation, and the uncertainties on the gas age are derived. The reason for choosing the uncertainties in this way is to account for the fact that $P(t)$ might not be Gaussian in all cases. The final ages for every sample along with the uncertainty are presented to the right in table 8.2.

After establishing this data analysis method for the NBI-PICE RECAP samples it was also used for the PSU RECAP measurements. In figure 8.7, δ^{18}O of RECAP from PSU and NBI-PICE are plotted with the estimated gas ages and the synthetic record.

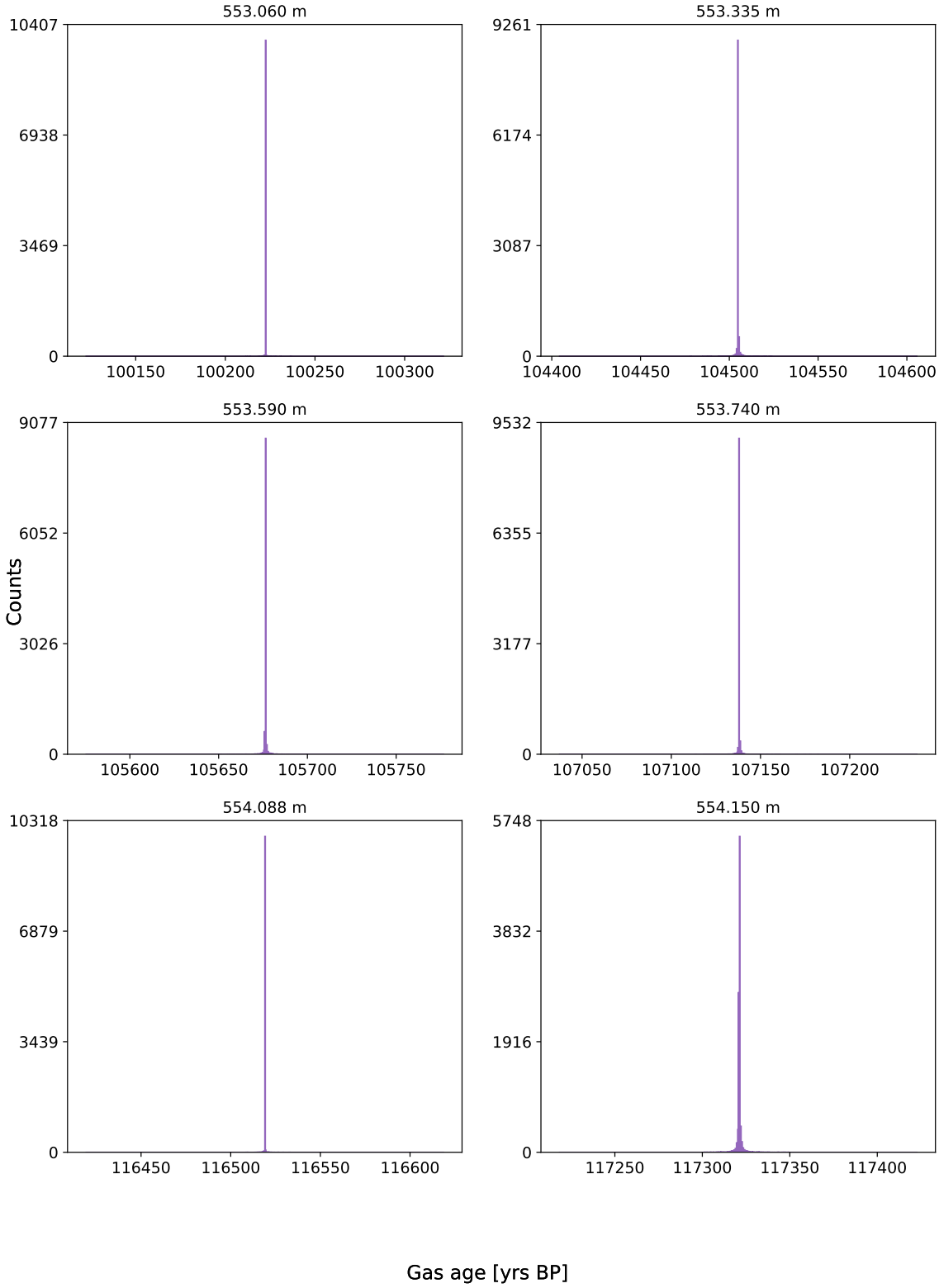

Figure 8.6: Histograms generated following $P(t)$.

Depth [m]	Gas age [years BP]		
	Mean	2.5% percentile	97.5% percentile
553.060	100226	100222	103341
553.335	104505	104504	104506
553.590	105678	105675	105681
553.740	107133	107130	107138
554.088	116524	116519	116529
554.150	117322	117318	117325

Table 8.2: Gas ages for the samples are shown alongside their 95% confidence intervals.

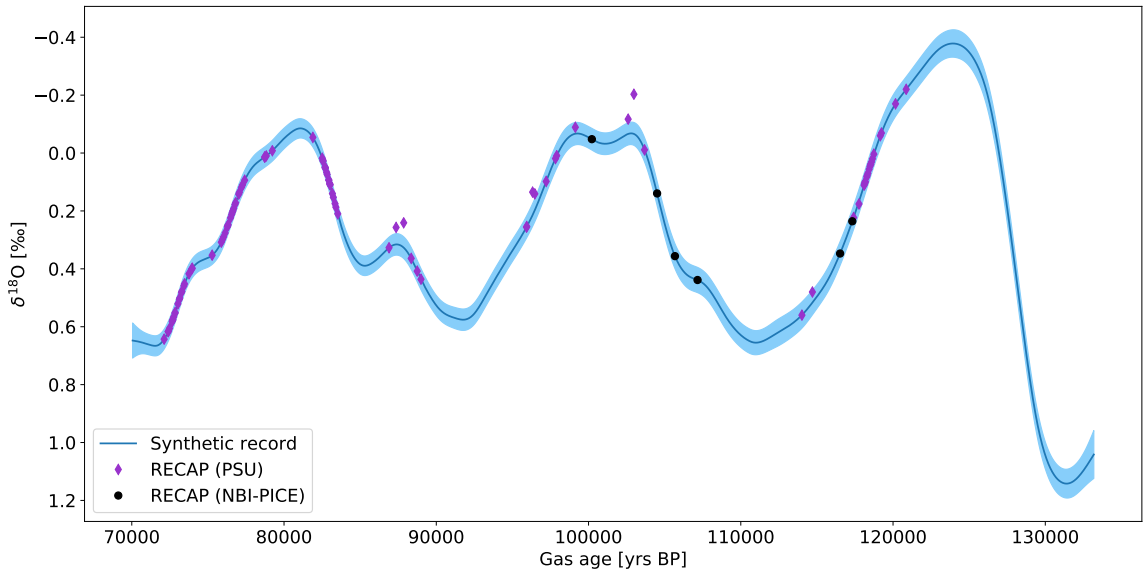

Figure 8.7: δ^{18}O of the NBI-PICE and PSU with estimated gas ages plotted alongside the synthetic record based on the EDML ice core.

8.3 Discussion

In table 8.2, the estimated uncertainties are much smaller than what is expected. This cannot be physical and indicates an underestimation of uncertainties. It can be debated whether the interpolation method used is suitable for the EDML data. Since the record does not have equal spacing in depth between every measurement, the different regions will be weighted differently. The `csaps` function allows for a smoothing parameter dependending on the average distance between the gas ages. This method for finding the smoothing parameter has been followed. Including weights for the EDML data dependent on how scarce data is in a region is a possible improvement upon the method.

A preliminary time scale for the RECAP core [Simonsen et al., 2019] with respect to Greenland Ice Core Chronology 2005 (GICC05) [Rasmussen et al., 2006] has been established based on measured markers in the ice such as dust contents or other gas measurements. At the depth of the six RECAP measurements, there are some tie points matching the depth of the core to the gas age. These are based on gas-correlations between the NGRIP ice core and RECAP ice core by CH_4 and $\delta^{18}O$ air measurements.

In figure 8.8, the depth of the samples from PSU and NBI-PICE are plotted against the estimated gas ages. In the same figure the tie markers from GICC05 are plotted in red.

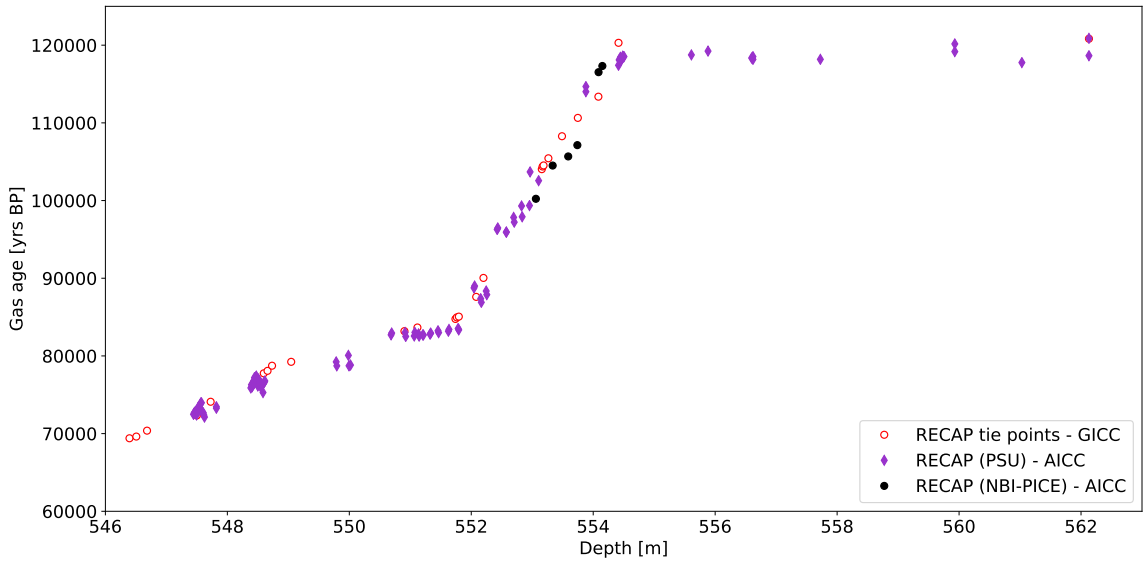

Figure 8.8: Gas age estimates for the RECAP ice core measurements from PSU and NBI-PICE are plotted against depth. Tie markers from the GICC05 time scale are plotted for comparison.

Some of the NBI-PICE measurements indicate offsets between the GICC05 tie points and the estimated gas ages from this study. This might also be due to the fact that the RECAP measurements are synchronized to AICC12 while the original RECAP age scale is tied to GICC05.

Another explanation for this offset is that this project has underestimated the importance of additional corrections such as accounting for thermal fractionation, gas loss fractionation or bubble close off fractionation. These might change the obtained $\delta^{18}O$ which in turn alter the estimated gas ages to more closely resemble the GICC05 time scale.

For the PSU RECAP data, the estimated gas ages do not increase at greater depths than $\simeq$554 m. This could be due to folding at the base of the ice sheet. Another explanation is that the measured $\delta^{18}O$ at this depth should in reality be mapped onto the increase in $\delta^{18}O$ of the EDML record that is seen between 120-130 kyrs BP (figure 8.7). However, the estimated gas ages for the PSU data fit well with the deepest tie

point of the GICC05 record, and so it is assumed the gas age estimation method is robust. Additional synchronization markers such as CH_4 are necessary to improve the uncertainty on the preliminary RECAP MIS5-5e gas age established here.

9 | Conclusion and outlook

Through this project, the NBI-PICE setup for extracting ancient air from ice core samples and measure the $\delta^{18}O$ composition has been brought to a functioning state. Robust and automated procedures for gauging corrections to measurements and instrument tests have been developed. Measurements of $\delta^{18}O$ can be performed with a standard deviation of $\pm 0.03‰$, which is within previous measured millenial changes of $\delta^{18}O$.

Six samples from the RECAP ice core were successfully measured from the depth interval of about 553 m to 554 m and an increase in $\delta^{18}O$ seen around a depth of 554 m was verified. Gas ages of the samples have been estimated by mapping them onto the already established time scale for the Antarctic EDML ice core. The same method was also applied to measurements of $\delta^{18}O$ from PSU. Finally the obtained time scale for the RECAP ice core is compared to the GICC05 match points.

In its current state, the setup is able to extract, trap and measure three samples in one measurement day. To increase the capacity, the dip tubes need to be refurbished or replaced. The water trap T2 may be removed to decrease dead volume in the system, as T1 appears to have a great enough capacity to freeze out water of several samples without clogging.

It has been discussed whether the vacuum casing of the dip tubes should be evacuated by a separate LV pump to reduce the chance of contamination of the line. No such contamination has been evident by inspection of the line, but for future projects this could be implemented. It is also suggested to place an additional water trap in front of the turbomolecular pump to boost pumping efficiency [Oyabu et al., 2020].

To fully respect the identical treatment principle, a procedure for measuring standard gas on top of BFI must be implemented. This demands creating BFI that is completely gas free so no fractionation is evident.

Finally, it is important to verify the RECAP measurements by measuring duplicate samples from similar depths as well as independent synchronization markers such as CH_4.

Bibliography

Laurent Augustin, Carlo Barbante, Piers R.F. Barnes, Jean Marc Barnola, Matthias Bigler, Emiliano Castellano, Olivier Cattani, Jerome Chappellaz, Dorthe Dahl-Jensen, Barbara Delmonte, Gabrielle Dreyfus, Gael Durand, Sonia Falourd, Hubertus Fischer, Jacqueline Flückiger, Margareta E. Hansson, Philippe Huybrechts, Gérard Jugie, Sigfus J. Johnsen, Jean Jouzel, Patrik Kaufmann, Josef Kipfstuhl, Fabrice Lambert, Vladimir Y. Lipenkov, Geneviève C. Littot, Antonio Longinelli, Reginald Lorrain, Valter Maggi, Valerie Masson-Delmotte, Heinz Miller, Robert Mulvaney, Johannes Oerlemans, Hans Oerter, Giuseppe Orombelli, Frederic Parrenin, David A. Peel, Jean Robert Petit, Dominique Raynaud, Catherine Ritz, Urs Ruth, Jakob Schwander, Urs Siegenthaler, Roland Souchez, Bernhard Stauffer, Jorgen Peder Steffensen, Barbara Stenni, Thomas F. Stocker, Ignazio E. Tabacco, Roberto Udisti, Roderik S.W. van de Wal, Michiel van den Broeke, Jerome Weiss, Frank Wilhelms, Jan Gunnar Winther, Eric W. Wolff, and Mario Zucchelli. Eight glacial cycles from an Antarctic ice core. *Nature*, 429(6992), 2004. ISSN 00280836. doi: 10.1038/nature02599.

Eugeni Barkan and Boaz Luz. High-precision measurements of 17O/16O and 18O/16O of O2 and O2/Ar ratio in air. *Rapid Communications in Mass Spectrometry*, 17(24), 2003. ISSN 09514198. doi: 10.1002/rcm.1267.

R. J. Barlow. *Statistics: A Guide to the Use of Statistical Methods in the Physical Sciences*, volume 33. John Wiley & Sons Ltd., 1991. doi: 10.2307/1269014.

M. O. Battle, J. P. Severinghaus, E. D. Sofen, D. Plotkin, A. J. Orsi, M. Aydin, S. A. Montzka, T. Sowers, and P. P. Tans. Controls on the movement and composition of firn air at the West Antarctic Ice Sheet Divide. *Atmospheric Chemistry and Physics*, 11(21), 2011. ISSN 16807316. doi: 10.5194/acp-11-11007-2011.

Michael Bender, Todd Sowers, Mary Lynn Dickson, Joseph Orchardo, Pieter Grootes, Paul A. Mayewski, and Debra A. Meese. Climate correlations between Greenland and Antarctica during the past 100,000 years. *Nature*, 372(6507), 1994a. ISSN 00280836. doi: 10.1038/372663a0.

Michael L. Bender. Orbital tuning chronology for the Vostok climate record supported by trapped gas composition. *Earth and Planetary Science Letters*, 204(1-2), 2002. ISSN 0012821X. doi: 10.1016/S0012-821X(02)00980-9.

Michael L. Bender, Pieter P. Tans, J. Taylor Ellis, Joseph Orchardo, and Karleugen Habfast. A high precision isotope ratio mass spectrometry method for measuring the O2 N2 ratio of air. *Geochimica et Cosmochimica Acta*, 58(21), 1994b. ISSN 00167037. doi: 10.1016/0016-7037(94)90205-4.

Bernhard Bereiter, Kenji Kawamura, and Jeffrey P. Severinghaus. New methods for measuring atmospheric heavy noble gas isotope and elemental ratios in ice core samples. *Rapid Communications in Mass Spectrometry*, 32(10):801–814, 5 2018. ISSN 10970231. doi: 10.1002/rcm.8099.

T. Blunier and E. J. Brook. Timing of millennial-scale climate change in antarctica and greenland during the last glacial period. *Science*, 291(5501), 2001. ISSN 00368075. doi: 10.1126/science.291.5501.109.

T. Blunier, M. L. Bender, B. Barnett, and J. C. Von Fischer. Planetary fertility during the past 400 ka based on the triple isotope composition of O2 in trapped gases from the Vostok ice core. *Climate of the Past*, 8(5), 2012. ISSN 18149324. doi: 10.5194/cp-8-1509-2012.

Thomas Blunier and Jakob Schwander. Gas enclosure in ice: age difference and fractionation. *Physics of Ice Core Records*, 2000.

Thomas Blunier, Bruce Barnett, Michael L. Bender, and Melissa B. Hendricks. Biological oxygen productivity during the last 60,000 years from triple oxygen isotope measurements. *Global Biogeochemical Cycles*, 16(3), 2002. ISSN 08866236. doi: 10.1029/2001gb001460.

Edward J. Brook and Christo Buizert. Antarctic and global climate history viewed from ice cores, 2018. ISSN 14764687.

E. Capron, A. Landais, B. Lemieux-Dudon, A. Schilt, V. Masson-Delmotte, D. Buiron, J. Chappellaz, D. Dahl-Jensen, S. Johnsen, M. Leuenberger, L. Loulergue, and H. Oerter. Synchronising EDML and NorthGRIP ice cores using δ18O of atmospheric oxygen (δ18Oatm) and CH4 measurements over MIS5 (80-123 kyr). *Quaternary Science Reviews*, 29(1-2), 2010. ISSN 02773791. doi: 10.1016/j.quascirev.2009.07.014.

D. Dahl-Jensen, M. R. Albert, A. Aldahan, N. Azuma, D. Balslev-Clausen, M. Baumgartner, A. M. Berggren, M. Bigler, T. Binder, T. Blunier, J. C. Bourgeois, E. J. Brook, S. L. Buchardt, C. Buizert, E. Capron, J. Chappellaz, J. Chung, H. B. Clausen, I. Cvijanovic, S. M. Davies, P. Ditlevsen, O. Eicher, H. Fischer, D. A. Fisher, L. G. Fleet, G. Gfeller, V. Gkinis, S. Gogineni, K. Goto-Azuma, A. Grinsted, H. Gudlaugsdottir, M. Guillevic, S. B. Hansen, M. Hansson, M. Hirabayashi, S. Hong, S. D. Hur, P. Huybrechts, C. S. Hvidberg, Y. Iizuka, T. Jenk, S. J. Johnsen, T. R. Jones, J. Jouzel, N. B. Karlsson, K. Kawamura, K. Keegan, E. Kettner, S. Kipfstuhl, H. A. Kjær, M. Koutnik, T. Kuramoto, P. Köhler, T. Laepple, A. Landais, P. L. Langen, L. B. Larsen, D. Leuenberger, M. Leuenberger, C. Leuschen, J. Li, V. Lipenkov, P. Martinerie, O. J. Maselli, V. Masson-Delmotte,

J. R. McConnell, H. Miller, O. Mini, A. Miyamoto, M. Montagnat-Rentier, R. Mulvaney, R. Muscheler, A. J. Orsi, J. Paden, C. Panton, F. Pattyn, J. R. Petit, K. Pol, T. Popp, G. Possnert, F. Prié, M. Prokopiou, A. Quiquet, S. O. Rasmussen, D. Raynaud, J. Ren, C. Reutenauer, C. Ritz, T. Röckmann, J. L. Rosen, M. Rubino, O. Rybak, D. Samyn, C. J. Sapart, A. Schilt, A. M.Z. Schmidt, J. Schwander, S. Schüpbach, I. Seierstad, J. P. Severinghaus, S. Sheldon, S. B. Simonsen, J. Sjolte, A. M. Solgaard, T. Sowers, P. Sperlich, H. C. Steen-Larsen, K. Steffen, J. P. Steffensen, D. Steinhage, T. F. Stocker, C. Stowasser, A. S. Sturevik, W. T. Sturges, A. Sveinbjörnsdottir, A. Svensson, J. L. Tison, J. Uetake, P. Vallelonga, R. S.W. Van De Wal, G. Van Der Wel, B. H. Vaughn, B. Vinther, E. Waddington, A. Wegner, I. Weikusat, J. W.C. White, F. Wilhelms, M. Winstrup, E. Witrant, E. W. Wolff, C. Xiao, and J. Zheng. Eemian interglacial reconstructed from a Greenland folded ice core. *Nature*, 493(7433), 2013. ISSN 00280836. doi: 10.1038/nature11789.

G. Dongmann, H. W. Nürnberg, H. Förstel, and K. Wagener. On the enrichment of H218O in the leaves of transpiring plants. *Radiation and Environmental Biophysics*, 11(1), 1974. ISSN 0301634X. doi: 10.1007/BF01323099.

M. N. Dyonisius, V. V. Petrenko, A. M. Smith, Q. Hua, B. Yang, J. Schmitt, J. Beck, B. Seth, M. Bock, B. Hmiel, I. Vimont, J. A. Menking, S. A. Shackleton, D. Baggenstos, T. K. Bauska, R. H. Rhodes, P. Sperlich, R. Beaudette, C. Harth, M. Kalk, E. J. Brook, H. Fischer, J. P. Severinghaus, and R. F. Weiss. Old carbon reservoirs were not important in the deglacial methane budget. *Science*, 367(6480), 2020. ISSN 10959203. doi: 10.1126/science.aax0504.

Bradley Efron. Second Thoughts on the Bootstrap, 5 2003. ISSN 08834237.

C. Goujon, J. M. Barnola, and C. Ritz. Modelling the densification of polar firn including heat diffusion: Application to close-off characteristics and gas isotopic fractionation for Antarctica and Greenland sites. *Journal of Geophysical Research D: Atmospheres*, 108(24), 2003. ISSN 01480227. doi: 10.1029/2002jd003319.

Jürgen H. Gross and Colin F. Poole. *Mass Spectrometry. A Textbook, 3rd Edn*, volume 81. 2018. doi: 10.1007/s10337-017-3400-5.

Isabell Grzymala-Lubanski. δ 18 O of O 2 in RICE ice core. Technical report, University of Copenhagen, 2015.

Myriam Guillevic. *Characterisation of rapid climate changes through isotope analyses of ice and entrapped air in the NEEM ice core Academic advisors*. PhD thesis, 2013.

Robert D. Guy, Marilyn L. Fogel, and Joseph A. Berry. Photosynthetic fractionation of the stable isotopes of oxygen and carbon. *Plant Physiology*, 101(1), 1993. ISSN 00320889. doi: 10.1104/pp.101.1.37.

Yael Helman, Eugeni Barkan, Doron Eisenstadt, Boaz Luz, and Aaron Kaplan. Fractionation of the three stable oxygen isotopes by oxygen-producing and oxygen-consuming reactions in photosynthetic organisms. *Plant Physiology*, 138(4), 2005. ISSN 00320889. doi: 10.1104/pp.105.063768.

Michael M. Herron and Chester C. Langway. Firn Densification: An Empirical Model. *Journal of Glaciology*, 25(93):373–385, 1980. ISSN 0022-1430. doi: 10.3189/s0022143000015239. URL `https://www.cambridge.org/core`.

Christof Huber and Markus Leuenberger. Measurements of isotope and elemental ratios of air from polar ice with a new on-line extraction method. *Geochemistry, Geophysics, Geosystems*, 5(10), 2004. ISSN 15252027. doi: 10.1029/2004GC000766.

A. Landais, V. Masson-Delmotte, N. Combourieu Nebout, J. Jouzel, T. Blunier, M. Leuenberger, D. Dahl-Jensen, and S. Johnsen. Millenial scale variations of the isotopic composition of atmospheric oxygen over Marine Isotopic Stage 4. *Earth and Planetary Science Letters*, 258(1-2), 2007. ISSN 0012821X. doi: 10.1016/j.epsl.2007.03.027.

A. Lane and Malcolm Dole. Fractionation of oxygen isotopes during respiration. *Science*, 123(3197), 1956. ISSN 00368075. doi: 10.1126/science.123.3197.574.

H. Linke, B. J. Alemán, L. D. Melling, M. J. Taormina, M. J. Francis, C. C. Dow-Hygelund, V. Narayanan, R. P. Taylor, and A. Stout. Self-propelled leidenfrost droplets. *Physical Review Letters*, 96(15), 2006. ISSN 00319007. doi: 10.1103/PhysRevLett.96.154502.

Boaz Luz and Eugeni Barkan. The isotopic ratios 17O/16O and 18O/16O in molecular oxygen and their significance in biogeochemistry. *Geochimica et Cosmochimica Acta*, 69(5):1099–1110, 3 2005. ISSN 00167037. doi: 10.1016/j.gca.2004.09.001.

Boaz Luz, Eugeni Barkan, Michael L. Bender, Mark H. Thiemens, and Kristie A. Boering. Triple-isotope composition of atmospheric oxygen as a tracer of biosphere productivity. *Nature*, 400(6744), 1999. ISSN 00280836. doi: 10.1038/22987.

P. Martinerie, V. Y. Lipenkov, D. Raynaud, J. Chappellaz, N. I. Barkov, and C. Lorius. Air content paleo record in the Vostok ice core (Antarctica): a mixed record of climatic and glaciological parameters. *Journal of Geophysical Research*, 99(D5), 1994. ISSN 01480227. doi: 10.1029/93jd03223.

Patricia Martinerie, Dominique Raynaud, David M. Etheridge, Jean Marc Barnola, and Danièle Mazaudier. Physical and climatic parameters which influence the air content in polar ice. *Earth and Planetary Science Letters*, 112(1-4), 1992. ISSN 0012821X. doi: 10.1016/0012-821X(92)90002-D.

V. Masson-Delmotte, H. C. Steen-Larsen, P. Ortega, D. Swingedouw, T. Popp, B. M. Vinther, H. Oerter, A. E. Sveinbjornsdottir, H. Gudlaugsdottir, J. E. Box, S. Falourd, X. Fettweis, H. Gallée, E. Garnier, V. Gkinis, J. Jouzel, A. Landais, B. Minster, N. Paradis, A. Orsi, C. Risi, M. Werner, and J. W.C. White. Recent changes in north-west Greenland climate documented by NEEM shallow ice core data and simulations, and implications for past-temperature reconstructions. *Cryosphere*, 9(4), 2015. ISSN 19940424. doi: 10.5194/tc-9-1481-2015.

Melissa Anne Headly. *Krypton and xenon in air trapped in polar ice cores: Paleoatmospheric measurements for estimating past mean ocean temperature and summer snowmelt frequency.* PhD thesis, University of California, San Diego, 2008.

Ikumi Oyabu, Kenji Kawamura, Kyotaro Kitamura, Remi Dallmayr, Akihiro Kitamura, Chikako Sawada, Jeffrey P. Severinghaus, Ross Beaudette, Anaïs Orsi, Satoshi Sugawara, Shigeyuki Ishidoya, Dorthe Dahl-Jensen, Kumiko Goto-Azuma, Shuji Aoki, and Takakiyo Nakazawa. New technique for high-precision, simultaneous measurements of CH4, N2O and CO2concentrations; Isotopic and elemental ratios of N2, O2and Ar; and total air content in ice cores by wet extraction. *Atmospheric Measurement Techniques*, 13(12), 2020. ISSN 18678548. doi: 10.5194/amt-13-6703-2020.

S. Olander Rasmussen, K. K. Andersen, A. M. Svensson, J. P. Steffensen, B. M. Vinther, H. B. Clausen, M. L. Siggaard-Andersen, S. J. Johnsen, L. B. Larsen, D. Dahl-Jensen, M. Bigler, R. Röthlisberger, H. Fischer, K. Goto-Azuma, M. E. Hansson, and U. Ruth. A new Greenland ice core chronology for the last glacial termination. *Journal of Geophysical Research Atmospheres*, 111(6), 2006. ISSN 01480227. doi: 10.1029/2005JD006079.

Corentin Reutenauer. *Measuring the triple O 2 isotopic composition of air trapped in ice cores and quantifying the causes of δ 18 O atm millennial scale variations.* PhD thesis, University of Copenhagen, 2016.

J. Schwander and B. Stauffer. Age difference between polar ice and the air trapped in its bubbles. *Nature*, 311(5981), 1984. ISSN 00280836. doi: 10.1038/311045a0.

J. Schwander, T. Sowers, J. M. Barnola, T. Blunier, A. Fuchs, and B. Malaizé. Age scale of the air in the summit ice: Implication for glacial-interglacial temperature change. *Journal of Geophysical Research Atmospheres*, 102(16), 1997. ISSN 01480227. doi: 10.1029/97jd01309.

Alan M. Seltzer, Christo Buizert, Daniel Baggenstos, Edward J. Brook, Jinho Ahn, Ji Woong Yang, and Jeffrey P. Severinghaus. Does δ18O of O2 record meridional shifts in tropical rainfall? *Climate of the Past*, 13(10):1323–1338, 10 2017. ISSN 18149332. doi: 10.5194/cp-13-1323-2017.

Jeffrey P. Severinghaus and Mark O. Battle. Fractionation of gases in polar ice during bubble close-off: New constraints from firn air Ne, Kr and Xe observations. *Earth and Planetary Science Letters*, 244(1-2), 2006. ISSN 0012821X. doi: 10.1016/j.epsl.2006.01.032.

Jeffrey P. Severinghaus, Alexi Grachev, Boaz Luz, and Nicolas Caillon. A method for precise measurement of argon 40/36 and krypton/argon ratios in trapped air in polar ice with applications to past firn thickness and abrupt climate change in Greenland and at Siple Dome, Antarctica. *Geochimica et Cosmochimica Acta*, 67 (3), 2003. ISSN 00167037. doi: 10.1016/S0016-7037(02)00965-1.

Jeffrey P. Severinghaus, Ross Beaudette, Melissa A. Headly, Kendrick Taylor, and Edward J. Brook. Oxygen-18 of O2 records the impact of abrupt climate change on the terrestrial biosphere. *Science*, 324(5933), 2009. ISSN 00368075. doi: 10.1126/science.1169473.

Marius Folden Simonsen, Giovanni Baccolo, Thomas Blunier, Alejandra Borunda, Barbara Delmonte, Robert Frei, Steven Goldstein, Aslak Grinsted, Helle Astrid Kjær, Todd Sowers, Anders Svensson, Bo Vinther, Diana Vladimirova, Gisela Winckler, Mai Winstrup, and Paul Vallelonga. East Greenland ice core dust record reveals timing of Greenland ice sheet advance and retreat. *Nature Communications*, 10(1), 2019. ISSN 20411723. doi: 10.1038/s41467-019-12546-2.

Todd Sowers and Michael Bender. Climate records covering the last deglaciation. *Science*, 269(5221), 1995. ISSN 00368075. doi: 10.1126/science.269.5221.210.

Todd Sowers, Ed Brook, David Etheridge, Thomas Blunier, Andreas Fuchs, Markus Leuenberger, Jerome Chappellaz, Jean Marc Barnola, Martin Wahlen, Bruce Deck, and Connie Weyhenmeyer. An interlaboratory comparison of techniques for extracting and analyzing trapped gases in ice cores. *Journal of Geophysical Research: Oceans*, 102(C12): 26527–26538, 11 1997. ISSN 21699291. doi: 10.1029/97JC00633. URL `https://agupubs.onlinelibrary.wiley.com/doi/full/10.1029/97JC00633` `https://agupubs.onlinelibrary.wiley.com/doi/abs/10.1029/97JC00633` `https://agupubs.onlinelibrary.wiley.com/doi/10.1029/97JC00633`.

Thermo Electron Corporation. DELTA V Plus Operating Manual. Technical report, 2005.

D. Veres, L. Bazin, A. Landais, H. Toyé Mahamadou Kele, B. Lemieux-Dudon, F. Parrenin, P. Martinerie, E. Blayo, T. Blunier, E. Capron, J. Chappellaz, S. O. Rasmussen, M. Severi, A. Svensson, B. Vinther, and E. W. Wolff. The Antarctic ice core chronology (AICC2012): An optimized multi-parameter and multi-site dating approach for the last 120 thousand years. *Climate of the Past*, 9(4):1733–1748, 2013. ISSN 18149324. doi: 10.5194/cp-9-1733-2013.

Roland A. Werner and Willi A. Brand. Referencing strategies and techniques in stable isotope ratio analysis, 2001. ISSN 09514198.

J. G. Ziegler and N. B. Nichols. Optimum settings for automatic controllers. *InTech*, 42(6), 1995. ISSN 0192303X.

A | Appendix

A.1 Peak shapes

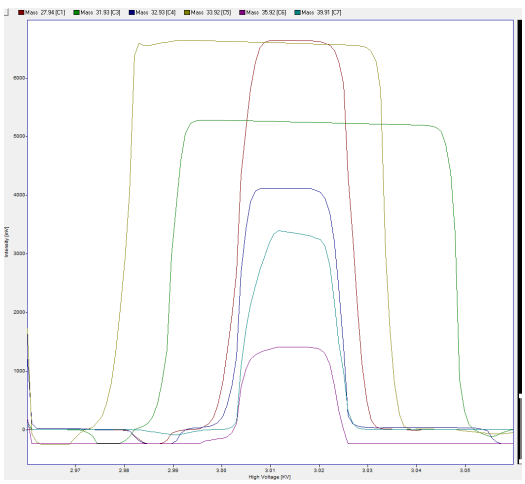

Extraction at 20%.

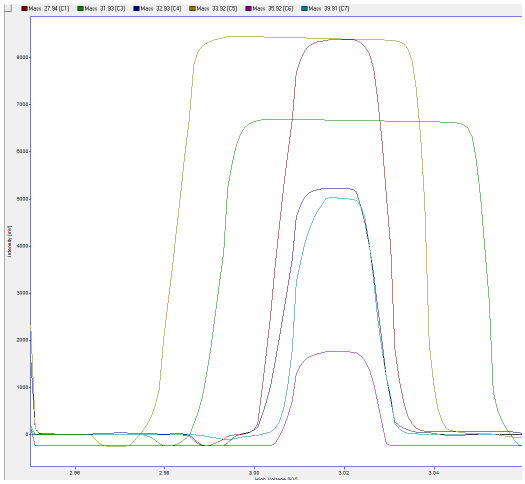

Extraction at 40%.

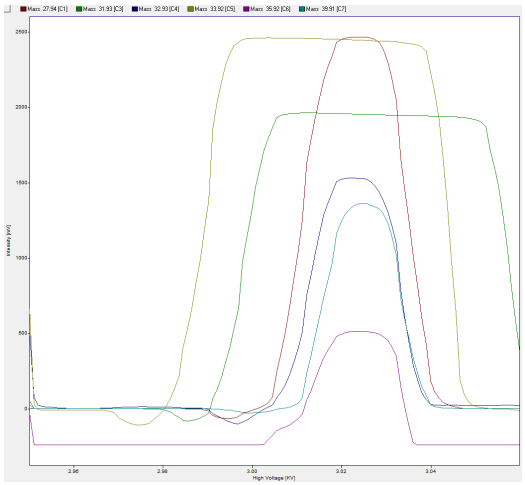

Extraction at 60%.

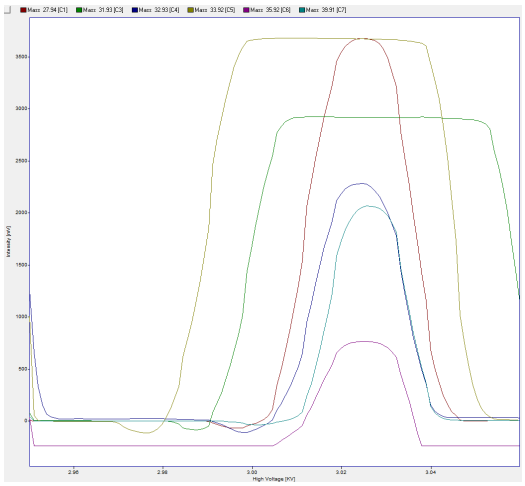

Extraction at 80%.

Figure A.1: Peak shapes of the $N_2/O_2/Ar$ configuration for different values of extraction. Vertical axes are signal intensities in mV, while the horizontal axes are the high voltage in kV.

A.2 NEEM measurements

Measurements of samples from the NEEM shallow ise core before the final configuration of the experimental setup.

Rod nr	δ^{18}O [‰]	δ^{15}N [‰]	$\delta^{18}O_{\text{grav corr}}$ [‰]
1	1.308	0.794	-0.281
6	0.498	0.170	0.1580
1	0.929	0.358	0.214
9	0.588	0.250	0.0886
8	0.308	0.120	0.0684
6	0.354	0.0539	0.247
1	0.868	0.349	0.169
3	0.242	0.151	-0.0602
4	0.312	0.0915	0.129
8	0.465	0.0206	0.423
6	0.742	0.261	0.220
8	0.473	0.0526	0.368
9	1.006	0.563	-0.119

Table A.1: Measurements of δ^{18}O and δ^{15}N from recent Holocene NEEM ice.